LAWRENCE
LIVERMORE
NATIONAL
LABORATORY

LLNL-TR-644936

Implementation of a Thermomechanical Model in Diablo for the Simulation of Selective Laser Melting

N. Hodge, R. M. Ferencz , J. M. Solberg

October 15, 2013

Disclaimer

This work performed under the auspices of the U.S. Department of Energy by Lawrence Livermore National Laboratory under Contract DE-AC52-07NA27344.

Abstract

Modeling of selective laser melting requires consideration of both heat transfer and solid mechanics. The present work describes continuum modeling of SLM as envisioned for eventually supporting part-scale modeling of this fabrication process to determine end-state information such as residual stress and distortion. The determination of the evolving temperatures is dependent on the state of the material (powder or solid), the specified heating, the value of each of the constitutive parameters, and the configuration. Similarly, the current mechanical configuration is dependent on the temperatures, the powder-solid state, and the values of the constitutive parameters. A multi-mechanics formulation is required to properly describe such problems. The current report describes the problem formulation, numerical method, and constitutive parameters necessary to solve such a problem. Additionally, various verification and example problems are presented to illustrate the Diablo implementation.

Contents

1 Introduction

This report documents the initial continuum thermo-mechanical modeling associated with the Laboratory's LDRD Strategic Initiative *Accelerated Certification For Additively Manufactured Metals (ACAMM)*. The effort described here aims to develop a part-level modeling capability to simulate the selective laser melting (SLM) process of additive manufacturing. The continuum modeling effort reported here consists of implementation of a thermal model, coupled to a mechanical model, along with appropriate verification, and presentation of various example problems. The model was implemented in the parallel, multi-physics finite element code Diablo [1].

The thermal model consists of the typical balance of thermal energy, with the associated boundary conditions, and the description of the phase change. The numerical formulation is the typical weighted residual formulation [2], solved in an incremental manner [3]. Several factors are extremely important in the modeling of SLM. The first factor is the representation of the laser heat source. There are numerous models for laser heating, with one of the most widely used being that of Goldak [4]. The Goldak model was originally conceived in the context of welding, and it is extremely flexible; indeed, it contains numerous arbitrary parameters, which must be calibrated for the problem of interest. A model in terms of the relevant constitutive and process parameters would be much more convenient to use, and we adopt a recent model aimed precisely at laser melting of powders. The other factor is the representation of the phase change. Good overviews of both the analytical problem and methods for solving it are presented in [5, 6].

The solid mechanics model consists of the typical balance laws, those being the ones for mass, linear momentum, and angular momentum. The numerical solution of the mechanical model is done in a Lagrangian frame, and using an incremental solution method. The details of solving these kinds of problems can be found elsewhere [7, 8, 9]. There are numerous methods for coupling independent physical models in order to solve multi-physics problems. The examples presented in the current document were all solved using a staggered solution scheme [7, 10, 11].

This document will proceed as follows: the first section presents a brief description of the physical problem. The next four sections will describe aspects of the thermal modeling, including the strong form of the problem, the numerical methods, validation of the model, and examples. The following four sections contain analogous information regarding the solid mechanics, including the strong form, the numerical implementation, a discussion of the material properties, and several examples, with comments regarding the physical coupling throughout.

2 Description of the Physical Problem

The SLM process of building a part is, conceptually, fairly simple. A thin bed of metal powder, tens of micron thick, is placed on a solid substrate. A laser passed over the powder, melting the powder and some portion of the substrate, so that the melted powder is attached to the substrate. Once a complete layer has been melted and attached, another layer of powder is added, and the process is repeated. Figure 1 presents a schematic of a laser melting a single layer of powder. In this figure, the laser is moving to the right, and the blue region at and to the left of the laser represents melted material. Consolidated material, either substrate or previously processed layers, is shown in gray at the bottom.

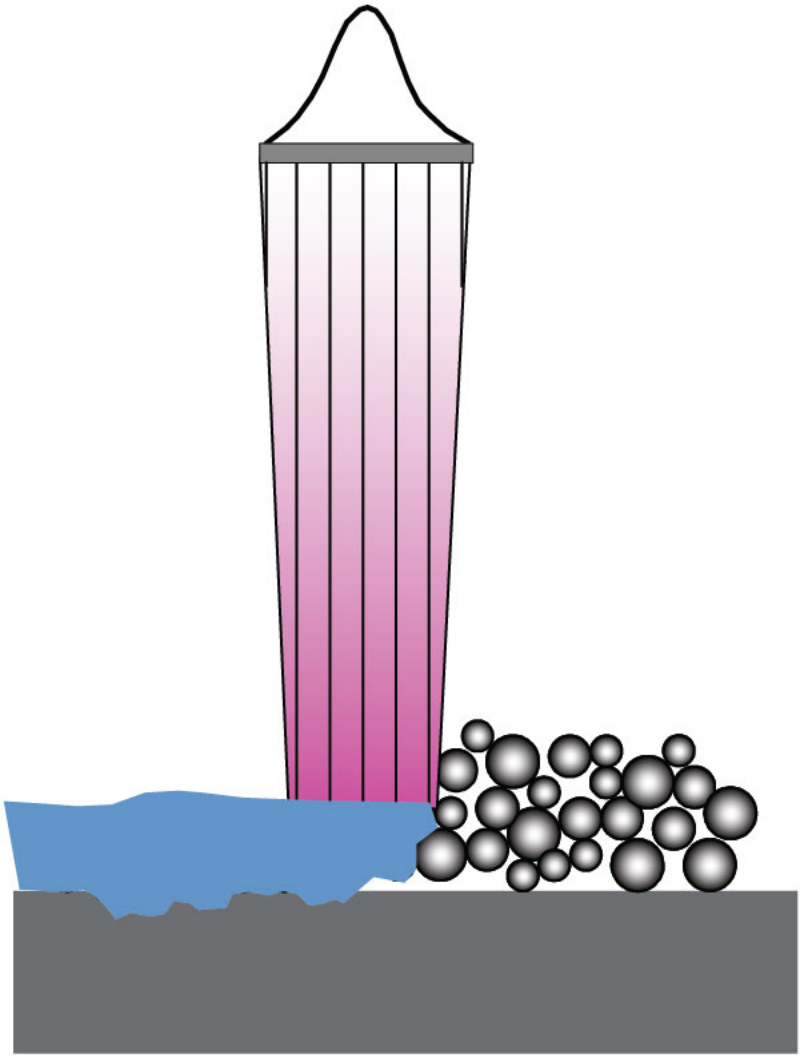

Figure 1: SLM process schematic

3 Thermal Problem Statement

The continuum thermal physics represented in the model described here can be considered as two separate (but related) phenomena: balance of thermal energy, and phase change. The balance of thermal energy is given by

$$\rho c_p \dot{T} = -\operatorname{div} \mathbf{q} + r, \text{ in } \Omega, \tag{1.1}$$

$$T(\mathbf{x}_T, t) = \bar{T}, \text{ on } \mathbf{x}_T \in \Gamma_T, \tag{1.2}$$

$$\mathbf{q}(\mathbf{x}_q, t) = \bar{\mathbf{q}}, \text{ on } \mathbf{x}_q \in \Gamma_q, \tag{1.3}$$

$$T(\mathbf{x}, 0) = T_0, \text{ on } \Omega \bigcup \partial\Omega, \tag{1.4}$$

where Γ_T is the portion of the boundary $\partial\Omega$ associated with essential boundary conditions, and Γ_q is the portion of the boundary associated with natural boundary conditions.

The phase change problem is described by the Stefan-Neumann equations:

$$T(\mathbf{x}_p, t) = T_p, \text{ on } \mathbf{x}_p \in \Gamma_p, \tag{2.1}$$

$$\left(\mathbf{k}_1 \frac{\partial T_1}{\partial \mathbf{x}} - \mathbf{k}_2 \frac{\partial T_2}{\partial \mathbf{x}}\right) \cdot \mathbf{n} = H\rho \frac{\partial \mathbf{x}_p}{\partial t} \cdot \mathbf{n}, \text{ on } \mathbf{x}_p \in \Gamma_p. \tag{2.2}$$

It is noted that the phase change is considered to occur along a surface internal to the body, which is denoted here by Γ_p. Additionally, the subscripts $(\cdot)_1$ and $(\cdot)_2$ denote the phases on opposite sides of the interface, H is the latent heat associated with the phase change, and $\mathbf{n}$ is a normal to the surface Γ_p. A more detailed description of the phase change problem, along with the analytical solution for the problem on a 1D domain, can be found in [5].

An important aspect of the thermal energy balance for this problem is the laser heating, which is represented by the r term in equation (1.1). One possibility for the heating model is that of Goldak, *et al.* [4], which was originally developed for the modeling of welding processes. However, in an attempt to have a model defined in terms of material properties more naturally associated with the problem at hand, the model described by Gusarov, *et al.* [12] was chosen; indeed, it was created precisely for the case of interest, *i.e.*, it was derived via the radiation transfer equation as applied to a powder bed. The model gives an expression for the volumetric heating r with units W/m^3 as

$$r(\xi_1, \xi_2, \xi_3) = -\beta_h Q_0 \frac{\partial u}{\partial \xi_3}, \tag{3}$$

where

$$Q_0 = \hat{Q}_0(Q_e, r_h, R),$$

$$u = \hat{u}\left(L, \rho_h, e^{\xi_3}\right),$$

where ξ_i are the coordinates in the moving frame of reference attached to the point that represents the the projection of the axis of the laser heat source onto the exterior surface of

the powder layer, and $r_h^2 = \xi_1^2 + \xi_2^2$ is the radial distance of a given point in the body from the axis projection point. The parameters necessary to calculate this model are as follows: the effective power of the heat source Q_e, the laser beam radius R (which is taken to be precisely half of the often used $D4\sigma$), the powder layer thickness L, the extinction coefficient β_h, and the hemispherical reflectivity of the powder ρ_h. It should be noted that the Gusarov heating model does not explicitly account for reflection, radiation, vaporization or any other heat rejection mechanisms on the surface of the powder. These effects are represented as a reduction of the nominal source magnitude to an effective source magnitude, Q_e.

4 Thermal Numerical Implementation

Given the relative ubiquity of information related to calculation of (1.1)-(1.4), no further mention will be made to the general solution of the problem here. Several comments regarding the specific case of concern will be made below.

For the problem at hand, the phase change represented via the Stefan-Neumann equations indeed represents a change between solid and liquid, but the phase information is used in a more subtle manner. The actual phases considered here consist of the "powder phase" (solid powder), and the "consolidated phase" (solid and liquid material without voids, taken together), *i.e.*, the term "consolidated", without any qualifier, will be used to refer to both the consolidated solid and consolidated liquid. This grouping of the phases provides the information necessary to drive the *irreversible* powder consolidation representation within the solid mechanics (as described later). The phase change between liquid and solid consolidated material is accounted for with variation of the material parameters as a function of temperature. Mathematically, the consolidation phase change calculations are associated with a phase variable, ϕ. Since the solid portions of the material can be either powder or consolidated, we allow for all of the continuum thermal material properties (*e.g.*, conductivity, heat capacity) to be a function of both temperature and phase.

Regarding the phase variable, we take ϕ_1 to be associated with the powder and ϕ_2 to be associated with the consolidated material. For each phase i, the phase variable may take on the values $0 \leq \phi_i \leq 1$. Additionally, at every point in the body, the constraint

$$\sum_i \phi_i = 1$$

is enforced. That is, the phase variables represent the local volume fraction of each of the phases.

Various references present useful discussion of the numerical implementation of the Stefan-Neumann equations [13, 14, 5]. It is first noted that, given the problem is defined at an internal interface of the body, it is conceivable that one might want to track the interface geometry precisely. An alternative is to formulate a method that tracks only the *volume*

within which the interface is located, which is the approach used here. The particular algorithmic treatment used in the current work was taken from Rolph and Bathe [15]. First, the expression for the balance of energy within a local volume containing a phase interface is

$$\Delta q \, dA = \pm \rho H \frac{dV}{dt},$$

where the $\pm$ are associated with the two possible directions of the phase change. The equation is characterized as being a balance between the net heat flux across the interface and the energy associated with the volumetric conversion of the material from one phase to another. While the previous expression is not quite the same as (2.2), the similarities are certainly evident. It is noted that since the numerical formulation only tracks volumes, it is sufficient to track the phase variables ϕ_i solely at element integration points. Continuing, the method goes about creating a body heating term r_p associated with the phase change, as follows:

$$\Delta r_p^{e,(i)} = - \int_{\Omega^e} \frac{1}{\Delta t} \rho^{(i-1)} c^{(i-1)} \left(T^{(i)} - T_p \right) dv,$$

where $(\cdot)^{(i)}$ is the i^{th} approximation (in the sense of an iterative solution strategy) to the quantity $(\cdot)$ at time $t + \Delta t$, $(\cdot)_p$ denotes quantities associated with the phase change, and $(\cdot)^e$ denotes quantities associated with element e. Since the equation above defines the iterate-wise increment, the total volumetric heating associated with the latent heat is defined as

$$r_p^{e,(i)} = r_p^{e,(i-1)} + \Delta r_p^{e,(i)},$$

and the consistency with the temperature-enthalpy relation is enforced by requiring that

$$\sum \Delta r_p^{e,(i)} = \pm \int_{\Omega^e} \frac{1}{\Delta t} \rho^{(i-1)} H \, dv.$$

Generally speaking, the method is described as follows (for, say, melting): the algorithm associates temperature increases past the melting temperature with a special body heating and simultaneously constrains the temperature to remain at T_m. Then, once the summation of the (incremental) special body heating is equal to the latent heat of the phase change, the temperature is again allowed to evolve per (1.1).

The phase change model currently implemented for this work is meant to describe the phase change of *elementally pure substances* (or alloys that exhibit congruent melting), *i.e.*, the phase change is assumed to take place at a single temperature, and not over a range of temperatures. As such, it is not strictly appropriate for modeling SLM of alloys. However, it was deemed sufficient for the initial implementation. Also, the method was implemented in order to only allow *one way* phase changes, *i.e.*, melting is allowed but "freezing" (in the sense of the consolidated material returning to the powdered form) is not.

Additionally, given the significant temperature excursions expected in the actual SLM process, we assumed that the changes in the thermal constitutive properties as a function of

temperature would significantly effect the results. Because of this, as well as the significant material property changes associated with the material consolidation, we believed that a consistent nonlinear formulation of the problem would aid in calculating a solution. This required adding the Fréchet derivative [16, 17, 18, 19] of the material terms to the linearized system of equations used to solve for the temperatures. In addition to the use of these nonlinear terms, various algorithmic controls were devised to help with the convergence properties of the implementation.

Given that the derivation presented in [12] resulted in an analytic expression for the laser heating that is fundamentally a function only of spatial coordinates and process and material properties, little needs to be said about the addition of the laser effects to the body heating term. However, it is again noted that the coordinates used in the Gusarov heating (3) are taken with respect to a moving frame of reference attached to the axis of the laser (as described above). Of course, this implies that the motion of the heat source is somehow specified. The motion of the laser is specified via a set of curves specifying $\mathbf{x}_{axis}(t)$, where each curve describes one spatial coordinate as a function of time. This is a general description of the motion, which provides flexibility for early model testing; in the future, the actual path data used in the additive manufacturing process will be used to define the path of the heat source.

5 Thermal Problem Parameters and Verification Results

In order to verify the implementation, results were compared to those presented in Gusarov, *et al.* [12]. The physical setup is that of a small block of material with a single layer of powder, upon which a single track of powder will be heated and transformed. The block is taken to be $0.6\,mm \times 0.2\,mm \times 0.2\,mm$. The laser spot will transit along the x direction, over the range $0 \leq x \leq 0.5\,mm$, and at $y = 0\,mm$, in order to utilize a symmetric domain. In the z direction, the top $0.050\,mm$ will be considered as powder, and the remainder will be taken to be material that is assumed to be consolidated at the outset (*e.g.*, the baseplate upon which the SLM is initiated). The nominal laser power is stated as $Q = 45\,W$, which Gusarov takes to correspond to an effective power $Q_e = 30\,W$. The size of the heat source is specified as $R = 0.060\,mm$. The boundary conditions are all insulated, except for that at $x = 0.6\,mm$, which is an essential boundary condition, that being $T = 303K$.

The material considered is 316L stainless steel, with properties given in Table 1; note that the subscripts $(\cdot)_p$ and $(\cdot)_c$ are used for the powder and consolidated phases, respectively. It is noted that, for the Gusarov comparisons, only the minimum amount of data necessary to capture relevant temperature dependence is used. As with Gusarov's simulation, no explicit effects due to evaporation are considered. In the immediate vicinity of the laser spot, bulk material temperatures often correspond to the gas phase. Local evaporation is just one of the factors contributing to use of an effective absorbed power $Q_e < Q$.

Table 1: Constitutive values from Gusarov, *et al.* [12]

Notation	Description	Value
$(\rho c)_p$	specific heat, powder	2.98@1600, 5.95@1700 $[MJ/m^3K@K]$
$(\rho c)_c$	specific heat, consolidated	4.25@1600, 5.95@1700 $[MJ/m^3K@K]$
k_p	thermal conductivity, powder	0.2@200, 0.3@1600, 20@1700 $[W/mK$ @ $K]$ [1]
k_c	thermal conductivity, consolidated	20 $[W/mK]$ [2]
ρ_h	hemispherical reflectivity	0.7
β_h	extinction coefficient	60,000 $[1/m]$
T_m	melting point	1700 $[K]$
H_m	latent heat of melting	2.18 $[GJ/m^3]$

[1] These values are approximate, due to significant variation as a function of factors which are not relevant to the current case.

[2] This value is approximate, due to a dearth of experimental data at the temperature of interest, *i.e.*, $1700\,K$.

The domain is discretized into $(240, 80, 80)$ linear hexahedral elements, which corresponds to $h^e = 0.0025\,mm$. Generalized trapezoidal time integration is used, along with auto time stepping, with typical time steps of $\sim 7 \times 10^{-7} s$ for robust nonlinear convergence.

The results presented here consist of two cases, those being calculated (1) without the effects of the consolidated solid-consolidated fluid phase change being considered, and (2) with this phase change being considered. Discussion of modification of the heat capacity in order to account for the phase change in the consolidated material, as well as a plot of the value of $c(T)$ as of the time of writing of this report, is presented in Section 9.

In the comparison between the Diablo results and those of Gusarov [12], we considered four factors: magnitude of the maximum temperature, and the length, width, and depth of the melt pool. These results are listed in Table 2, and illustrated in Figures 2 and 3. The test case corresponds to Figure 8(d) of Gusarov, *et al.* [12], for $\lambda = 3$[1] and laser scan speed $v_{source} = 120\,mm/s$. The results clearly indicate that consideration of the solid-fluid phase change within the consolidated material is important to obtain the correct melt pool length, while the other two dimensions seem relatively insensitive to its inclusion.

Table 2: Comparison of Diablo results to Gusarov, *et al.* [12]

Quantity	Gusarov	Diablo, case 1	Diablo, case 2
Maximum temperature $[K]$	4900	5000	5000
Length $[mm]$	0.300	0.167	0.263
Width $[mm]$	0.200	0.205	0.208
Depth $[mm]$	0.070	0.063	0.065

[1] λ is the optical thickness, defined as $\lambda = \beta_h L$.

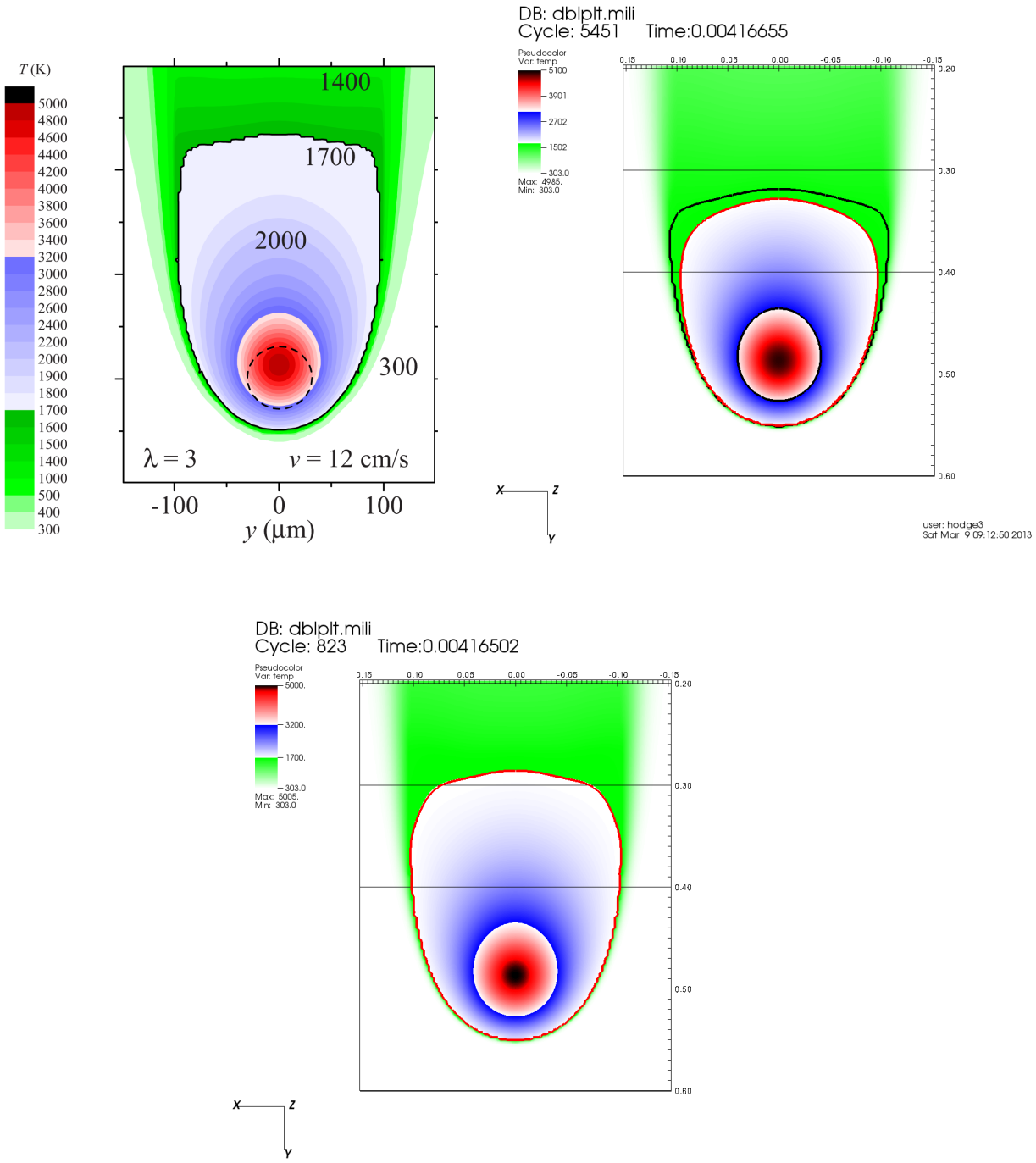

Figure 2: Surface temperature profiles for initial verification case, Gusarov (left), Diablo, case 1 (right), Diablo, case 2 (center below).

Next, the cross-sectional shape of the melt pool is displayed. Figure 3 shows a plot of the material boundaries, along with the temperature contour for $T = 1650K$. The figure illustrates good correlation of the melt pool depth and cross-sectional shape.

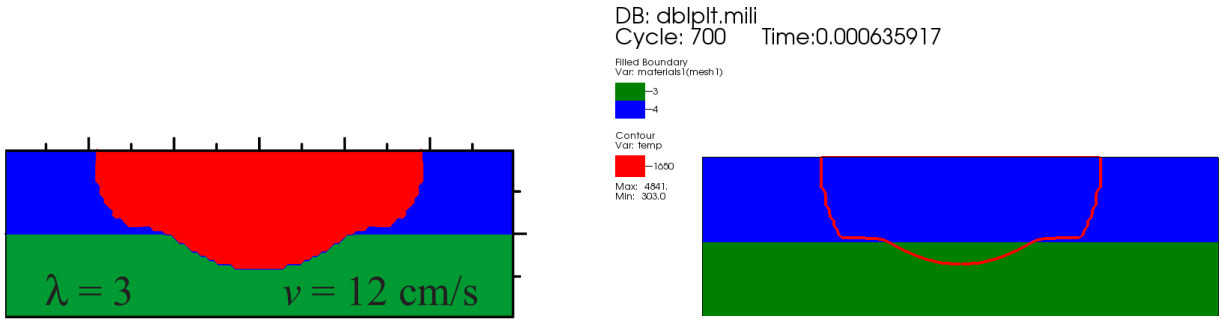

Figure 3: Melt pool cross-sections at $x = 0\,mm$, for $v_{source} = 120\,mm/s$, Gusarov (left) and Diablo (right). For Diablo results the element volumes are rendered in a constant color to match the color scheme of Gusarov while the perimeter is represented by a contour of constant $T = 1650\,K$ solidus temperature. The dimensional scale is the same for both cases.

Also shown is Figure 4, which depicts the value of the average phase variable, $\bar{\phi}$, where

$$\bar{\phi} = \phi_1 + 2\phi_2,$$

so that $\bar{\phi} = 1$ corresponds to powder (red) , and $\bar{\phi} = 2$ corresponds to consolidated material (blue). The solution time in Figure 4 is the same as that shown in Figure 3. Is is noted that, for the material that was consolidated at $t = 0$ (elements at and below the white dotted line), the phase algorithm is disabled, which is associated with a average phase $\bar{\phi} = 1$ by definition. Removal of the reflected portion of the domain and overlaying the melt pool boundary onto the plot of $\bar{\phi}$ provides another view of the infiltration of the melt pool into the initially consolidated material.

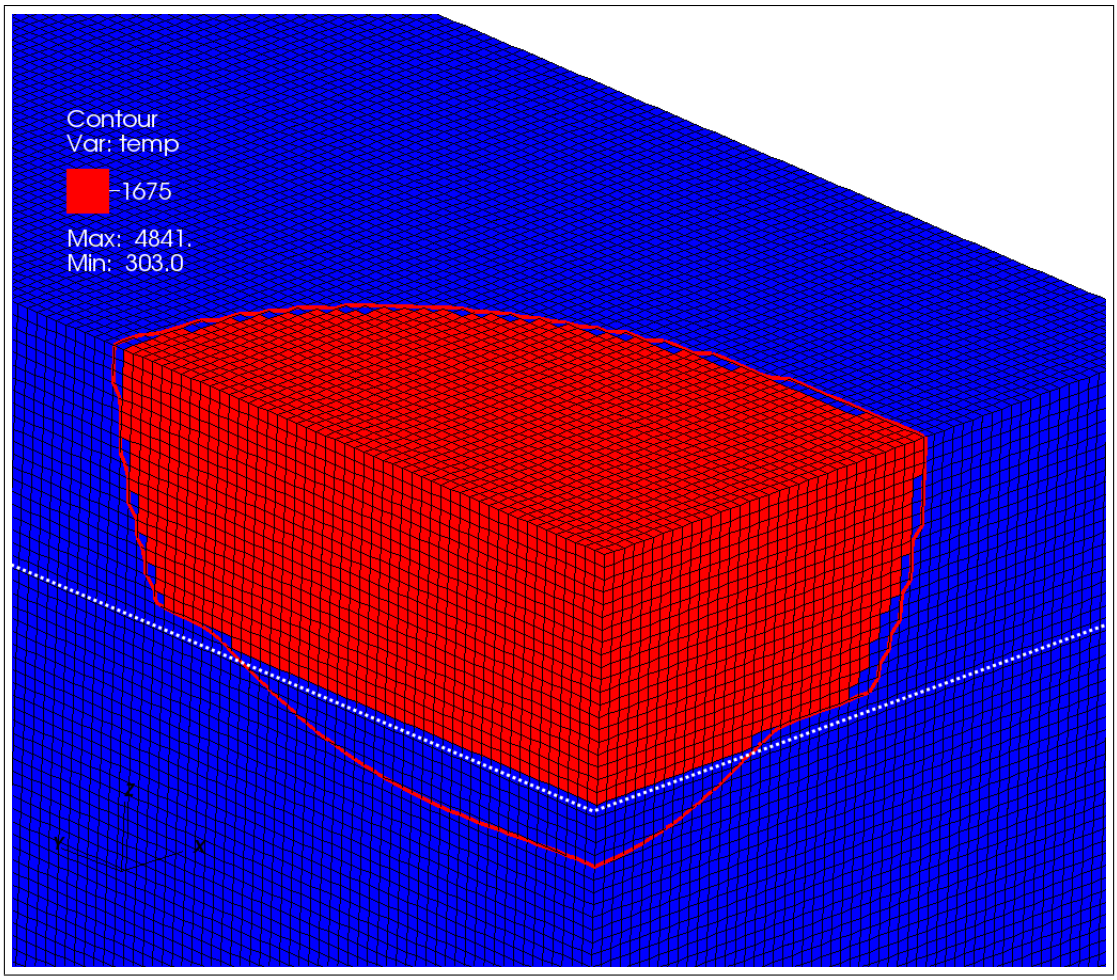

Figure 4: Illustration of melt pool geometry as represented by region of transformed powder (red) along with melt pool boundary, for $v_{source} = 120\,mm/s$.

Additional verification comparisons were also performed to ensure that various geometric aspects of the tail end of the melt pool were being properly captured by the model. Figure 5 corresponds to Figure 8(d) from Gusarov, *et al.* [12], with $\lambda = 3$ and $v_{source} = 240\,mm/s$. As per Gusarov's results, the shape of the heat-affected zone is narrower and longer overall, and in particular, the concave region at the tail is reasonably replicated. The concave region would appear to exist due to the lower conductivity of powder along the lateral edges, versus higher conductivity of the consolidated material toward the base and rear of the melt pool.

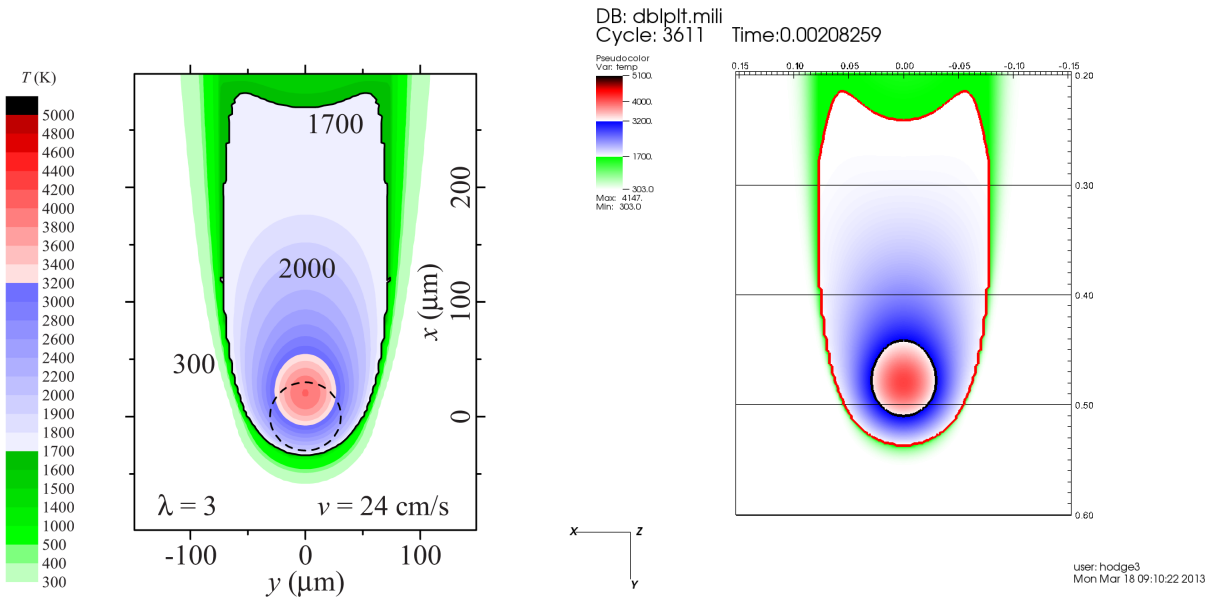

Figure 5: Surface temperature profiles for higher laser scan speed $v_{source} = 240\,mm/s$, Gusarov (left) and Diablo (right).

6 Thermal Examples

We used the above-described algorithm(s) to compute the solution to several additional example problems. The first example is a single track with process parameters of $Q_e = 250\,W$ and $v_{source} = 1600\,mm/s$, and powder layer thickness of $0.050\,mm$, which are among a group of parameter sets that are experimentally associated with low porosity after processing [20].

Figures 6 and 7 display the results of the calculation of the first example. For these examples, the beam radius is taken as $0.060\,mm$. The first of these figures shows the melt pool, with the red region indicating the consolidated region, and the blue region indicating unconsolidated powder. The particular time state shows the melt pool at its longest ($1.315\,mm$). This configuration represents a particular case, that being of the laser heating from the edge of a part. However, it does not represent the most general steady-state solution, that being of the melt pool in the interior of the surface, as the tail is influenced by the insulating boundary condition at the the plane $y = 0.0$. A future calculation will extend this domain ($y_{max} \geq 1.75$).

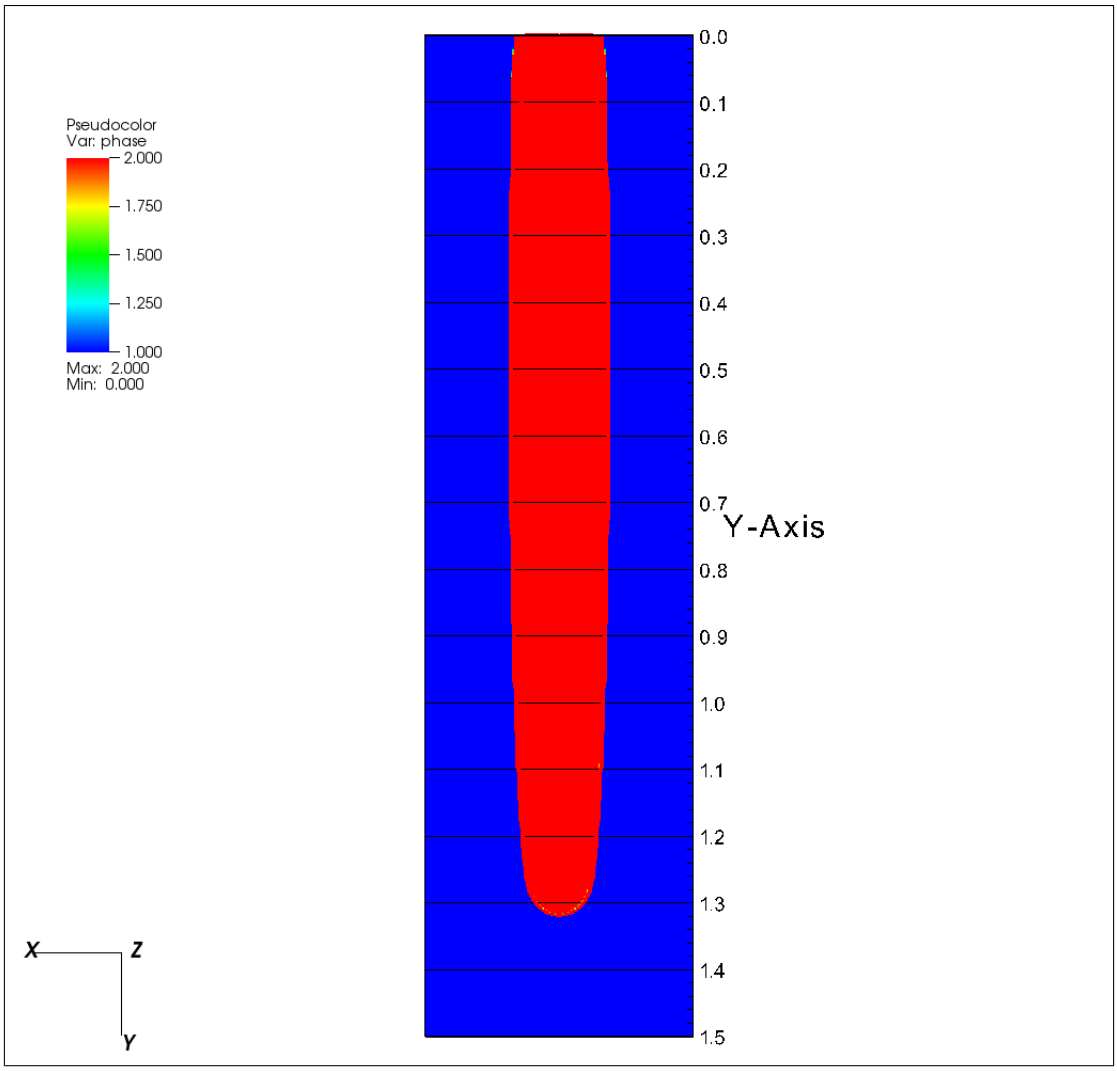

Figure 6: Value of average phase $\bar{\phi}$, along with melt pool boundary

Figure 7 depicts a detailed view of the leading edge of the melt pool. The figure shows an interesting feature of the results, that being the gap between the contour of $T = T_m$ and the leading edge of the melt pool. This is indicative of the time constant associated with the phase change, and likely results from the laser power and speed both being significantly higher than for the previous cases. Indeed, this effect is not seen in the verification cases in the previous section.

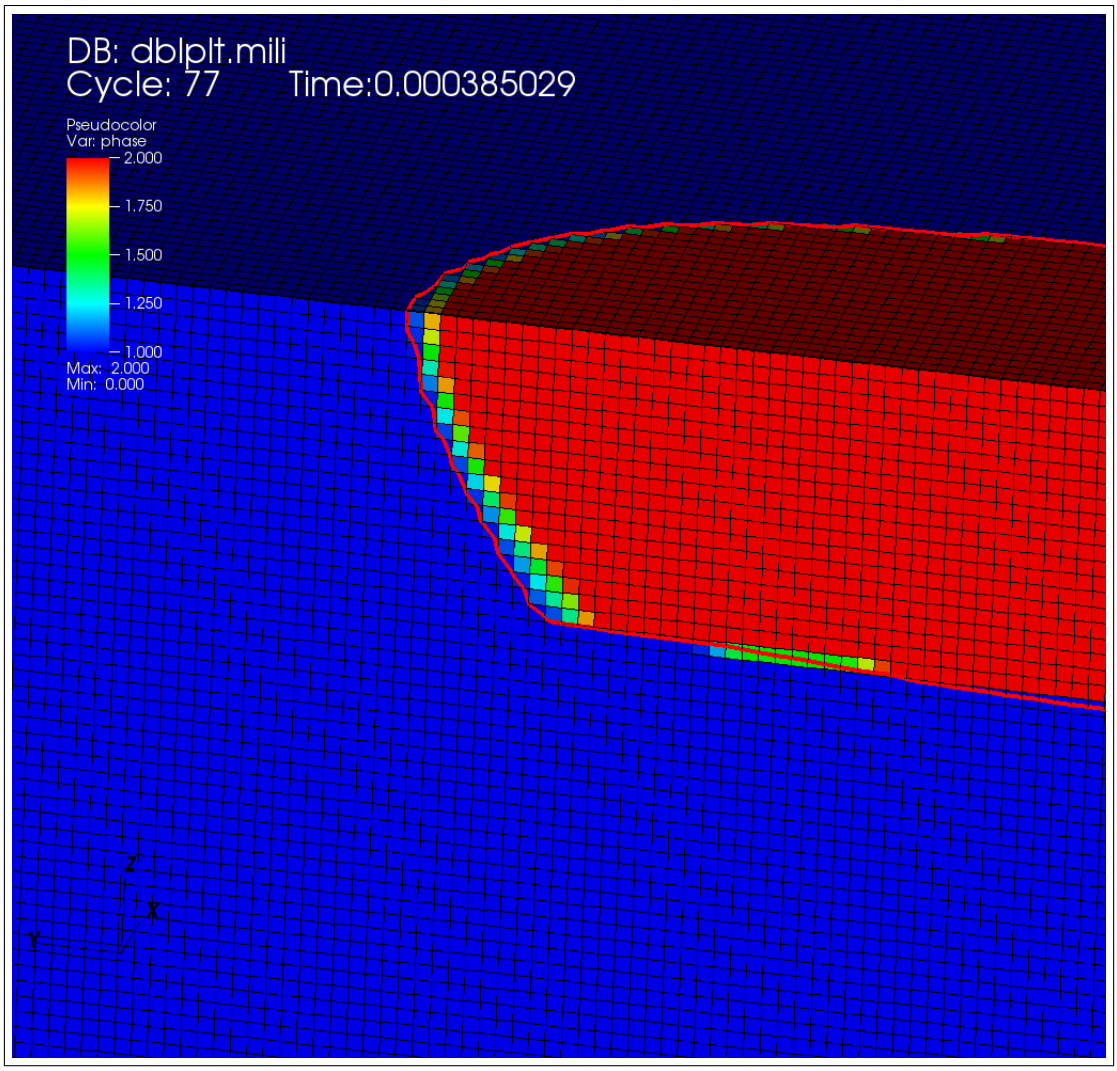

Figure 7: Close view of front end of melt pool, showing average phase $\bar{\phi}$

The final example consists of nine powder layers, with the first six of the layers being consolidated over only half of the part plan-form, so that consolidation of the final three layers results in the creation of an overhang. Figures 8-11 are a sequence of figures illustrating the initial transit of the heat source into the overhang region. The insulating nature of the powder below the overhang results in a significant enlargement of the melt pool, as well as increase of its maximum temperature. This, in turn, results in a locally phase-changed region that is up to three powder layers thick in places. Figure 10 also shows that the overhang remains liquid (*i.e.*, the melt pool splits into two distinct regions) as the laser transits back to the non-overhang region.

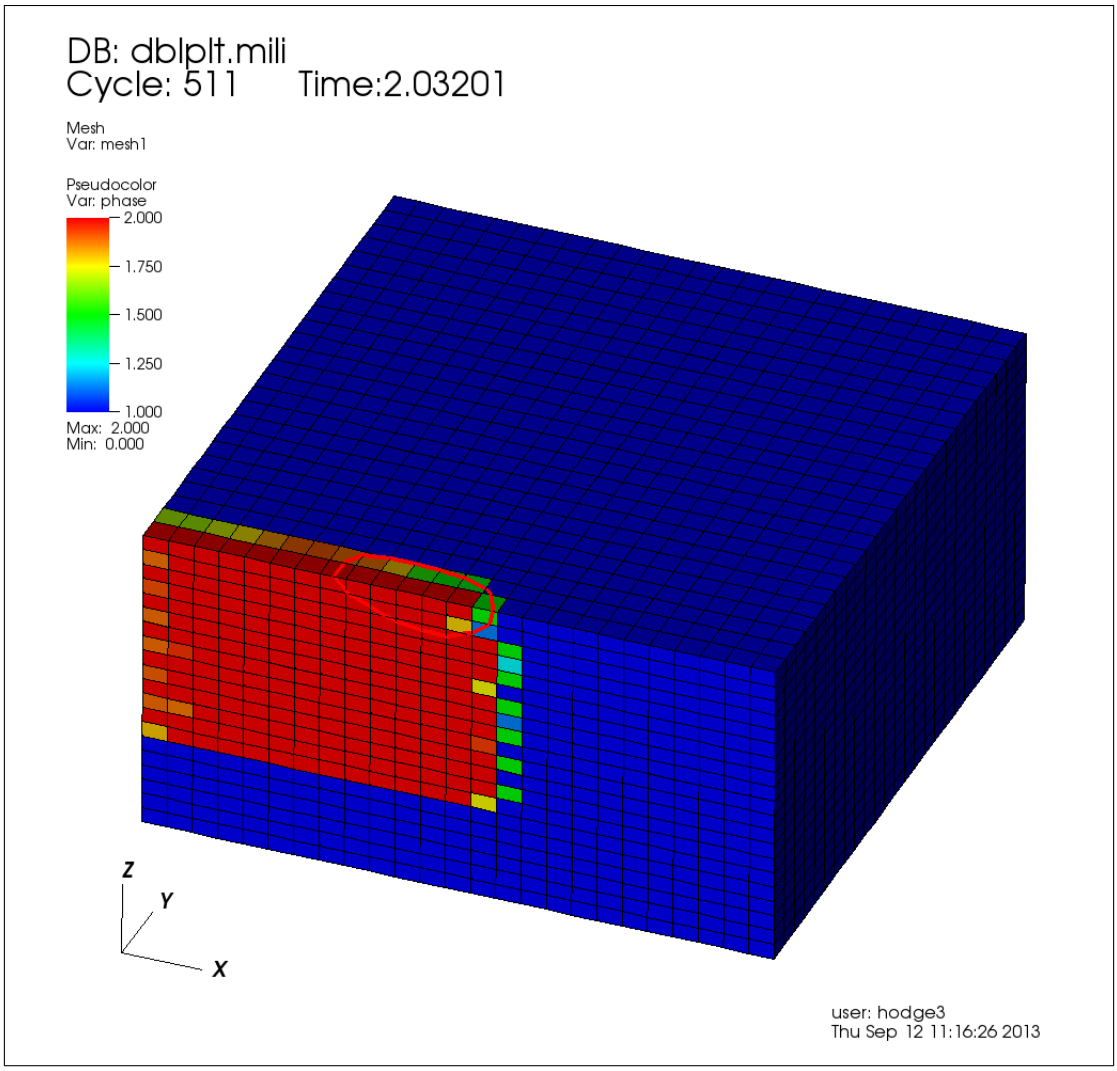

Figure 8: Overhang case: laser traveling to right, just before transiting into overhang region

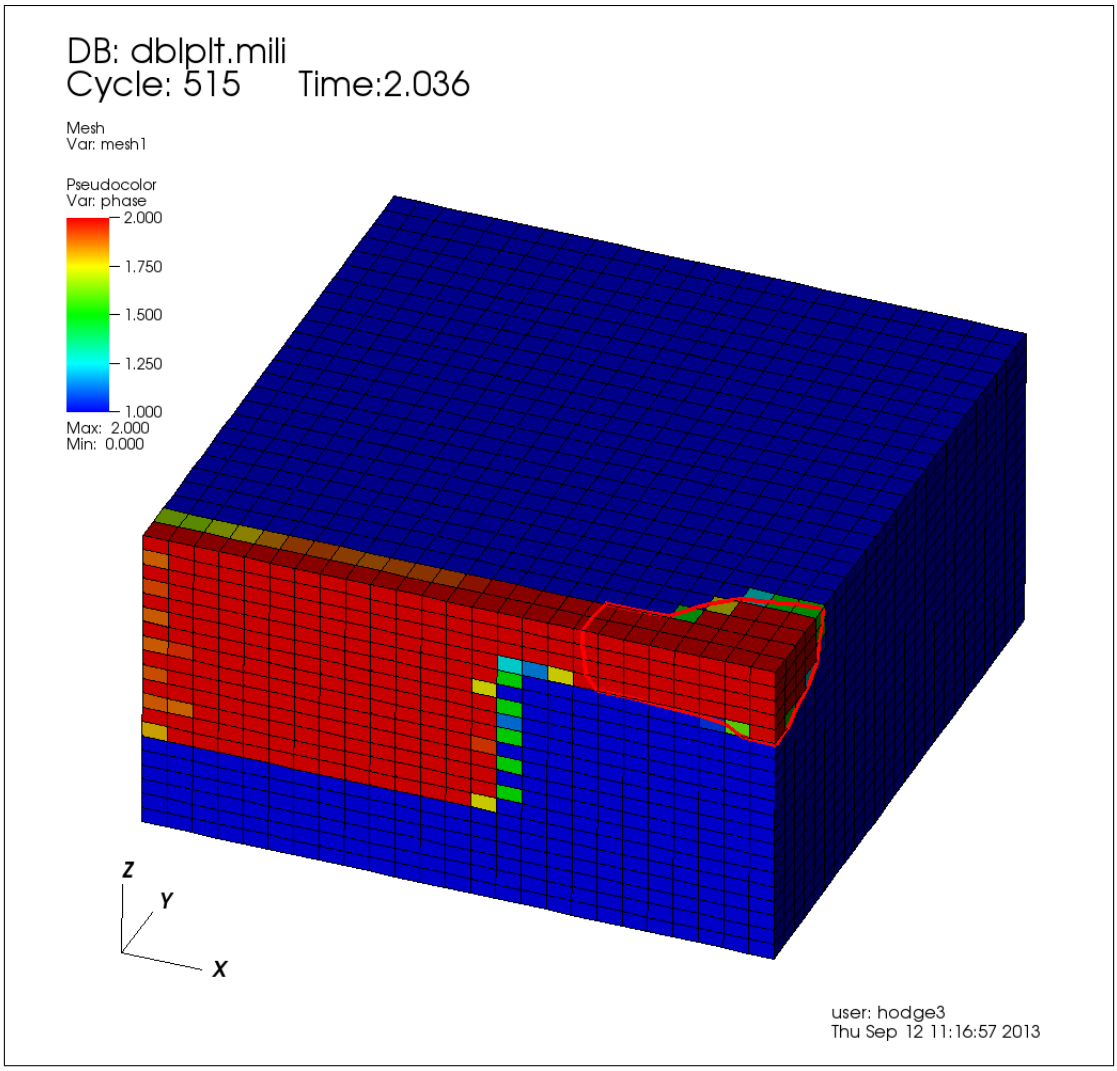

Figure 9: Overhang case: Volume of melt pool increasing, including melt pool reaching significantly deeper into powder than when over solid material

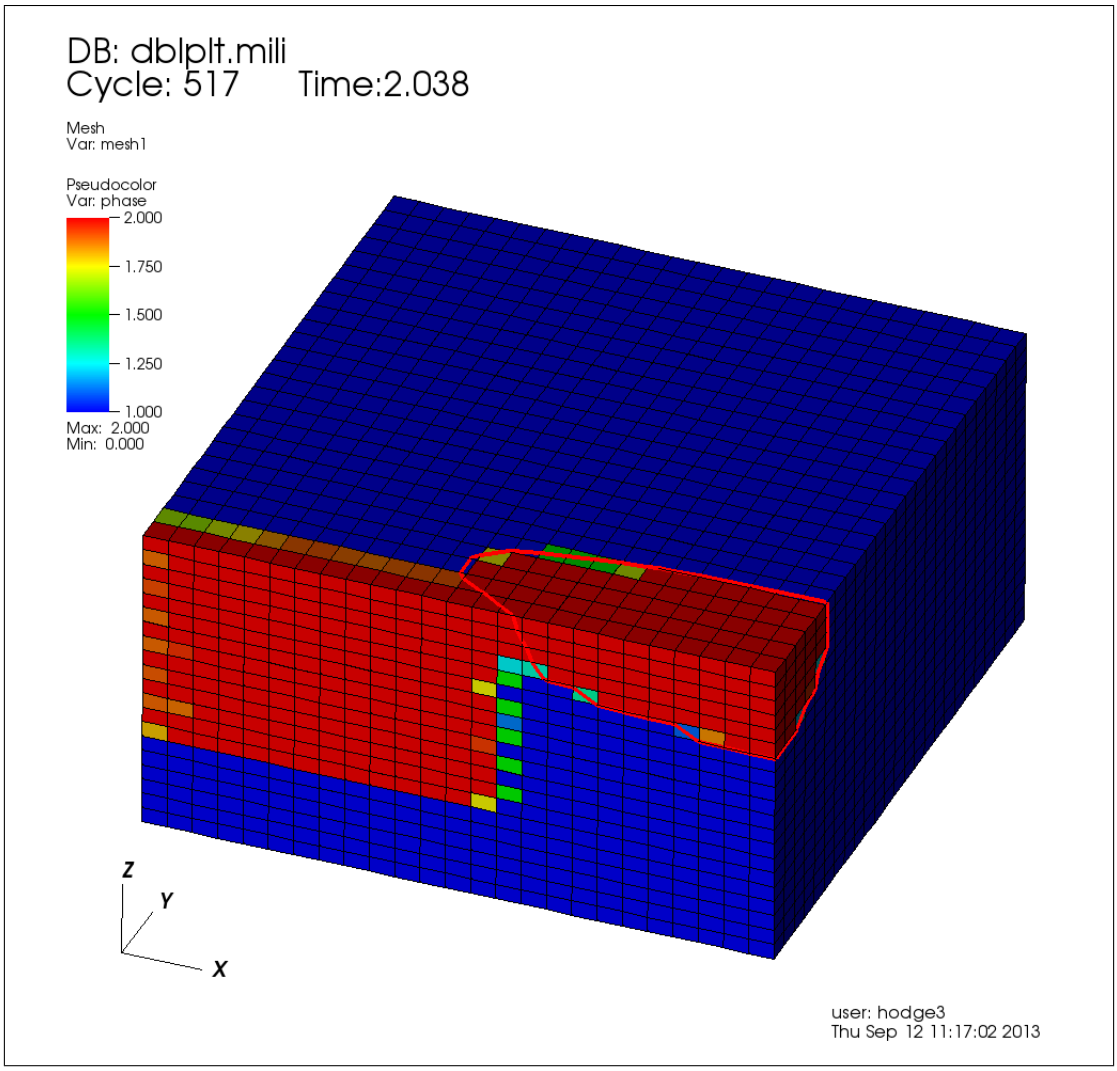

Figure 10: Overhang case: Laser now heading to the left, and melt pool volume still increasing

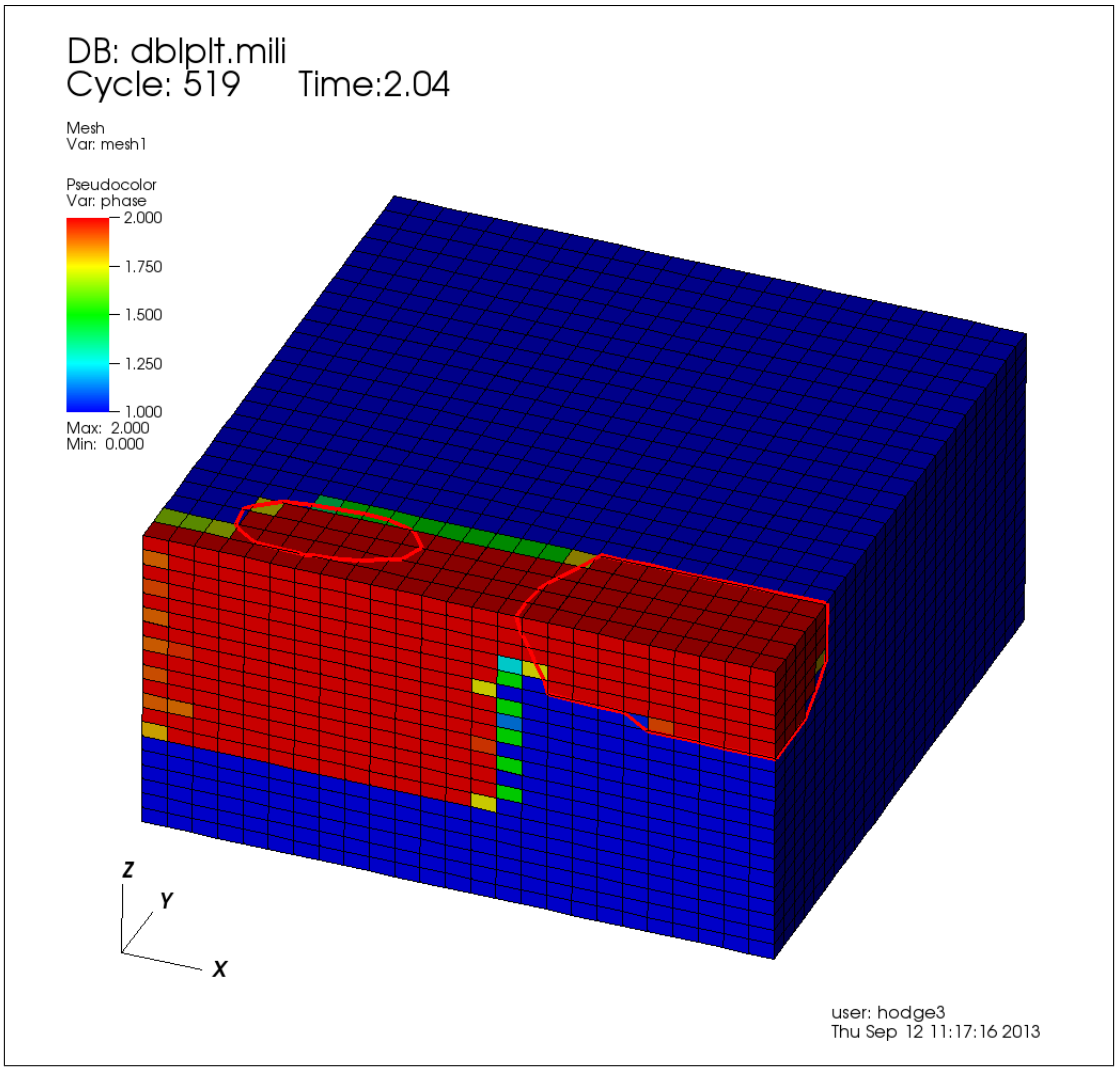

Figure 11: Overhang case: Laser now returned to non-overhang region, with separate melt pool segment remaining behind in overhang region

Finally, the temperature-time history shown in Figure 12 clearly indicates the higher temperature and longer exposure time experienced by a point in the overhang region. In this figure, the "bulk node" is in a layer with consolidated material directly under it. The higher heating of the overhang node is undoubtedly due to the insulating behavior of the unconsolidated powder below the overhang region. This is consistent with experimental results that report a larger melt pool with higher temperatures when creating an overhang via SLM. It is noted that peaks after the initial one (for each node) represent the effect of successive laser tracks.

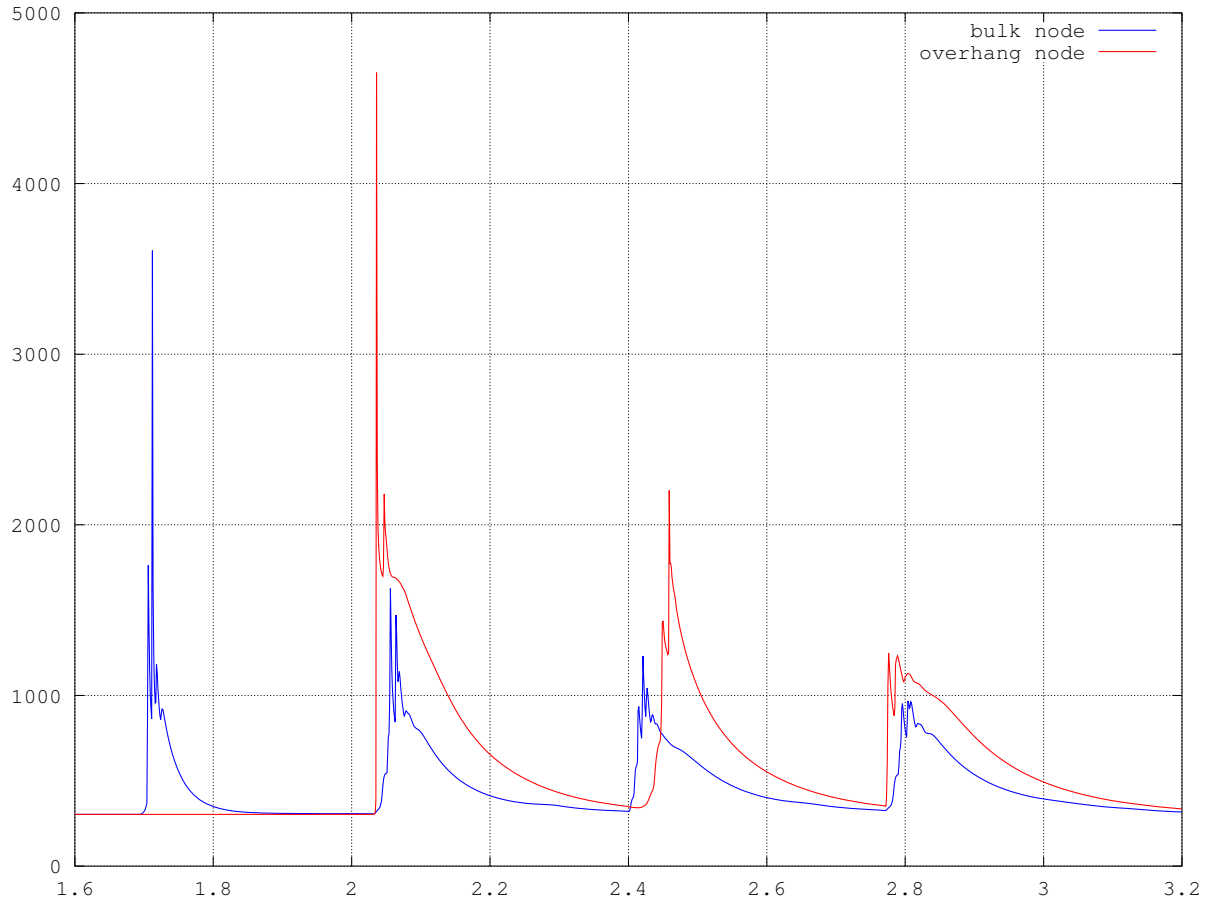

Figure 12: Temperature histories for two nodes in overhang case

7 Thermomechanical Problem Statement

The continuum solid physics centers around the balance of mass, the balance of linear momentum, and the balance of angular momentum. The first two of these equations (along with the attendant boundary and initial conditions) are stated as

$$\dot{\rho} = \rho \operatorname{div} \mathbf{v}, \text{ in } \Omega, \tag{4.1}$$

$$\rho \dot{\mathbf{v}} = \operatorname{div} \mathbf{T} + \rho \mathbf{b}, \text{ in } \Omega, \tag{4.2}$$

$$\mathbf{u}(\mathbf{x}_u, t) = \bar{\mathbf{u}}, \text{ on } \mathbf{x}_u \in \Gamma_u, \tag{4.3}$$

$$\mathbf{t}(\mathbf{x}_t, t) = \bar{\mathbf{t}}, \text{ on } \mathbf{x}_t \in \Gamma_t, , \tag{4.4}$$

$$\rho(\mathbf{x}, 0) = \rho_0, \text{ on } \Omega \bigcup \partial\Omega, \tag{4.5}$$

$$\mathbf{u}(\mathbf{x}, 0) = \mathbf{u}_0, \text{ on } \Omega \bigcup \partial\Omega, \tag{4.6}$$

$$\mathbf{t}(\mathbf{x}, 0) = \mathbf{t}_0, \text{ on } \Omega \bigcup \partial\Omega, \tag{4.7}$$

where Γ_u is the portion of the boundary $\partial\Omega$ associated with essential boundary conditions, and Γ_t is the portion of the boundary associated with natural boundary conditions. The balance of angular momentum is satisfied by the constraint $\mathbf{T} = \mathbf{T}^T$.

The coupling between the thermal and mechanical problems occurs through several mechanisms. First, the Cauchy stress $\mathbf{T}$ is not just a function of deformation $\mathbf{u}$, rather

$$\mathbf{T} = \hat{\mathbf{T}}(\operatorname{grad} \mathbf{u}, T, \phi_1, \phi_2).$$

Moreover, this functional dependence occurs in two manners. First, the material parameters that define the stress are a function of both temperature and phase (*e.g.*, Young's modulus $E = \hat{E}(T, \phi_1, \phi_2)$). Second, the strain contains constitutively defined parts that are functionally dependent on the temperature and the phases; this will be further described in the following paragraph. The final coupling mechanism is that the mechanical problem moves the mesh, which changes the problem domain for the thermal problem.

Our base assumption regarding the multi-phase kinematics is that the strains are the same for all phases,

$$\boldsymbol{\varepsilon} = \boldsymbol{\varepsilon}_1 = \boldsymbol{\varepsilon}_2.$$

Given that each phase has different material properties, this will result in a different stress for each phase. The total stress is defined as a volume-fraction weighted average:

$$\mathbf{T} = \phi_1 \mathbf{T}_1 + \phi_2 \mathbf{T}_2.$$

Regarding the thermomechanical coupling, in addition to the temperature and phase dependence of the material parameters, the strains have constitutively specified components, so that

$$\boldsymbol{\varepsilon} = \boldsymbol{\varepsilon}_u + \boldsymbol{\varepsilon}_T + \boldsymbol{\varepsilon}_\phi,$$

where

$$\boldsymbol{\varepsilon}_T = \left[\phi_1\alpha_1\left(T - T_{ref1}\right) + \phi_2\alpha_2\left(T - T_{ref2}\right)\right]\mathbf{I},$$
$$\boldsymbol{\varepsilon}_\phi = \left[\phi_1\beta_1 + \phi_2\beta_2\right]\mathbf{I},$$

and α_i, β_i are the coefficients of thermal and phase expansion (respectively) for phase i. We introduce the phase expansion to abstractly describe the volumetric kinematics of porosity loss as the powder melts and coalesces to a consolidated state. We do not attempt to describe the details of those behaviors, which are the subject of another modeling effort that is part of this LDRD-SI [21].

The constitutive relation for both of the phases is a phase-dependent, isotropic elastic-plastic, rate-based model. The stress update is specified as

$$\hat{\mathbf{T}}_{n+1} = \hat{\mathbf{T}}_n + \Delta\mathbf{D}\,\boldsymbol{\varepsilon}_{n,elastic} + \mathbf{D}_{n+\frac{1}{2}}\left(\Delta\boldsymbol{\varepsilon} - \Delta\boldsymbol{\varepsilon}_T - \Delta\boldsymbol{\varepsilon}_\phi - \Delta\boldsymbol{\varepsilon}_p\right),$$

where $\mathbf{D}$ is a fourth order tensor of material parameters, $\Delta\mathbf{D}$ accounts for the variation of the elastic material parameters, *i.e.*,

$$\Delta\mathbf{D} = \left.\frac{\partial\mathbf{D}}{\partial E}\right|_{n+\frac{1}{2}}\Delta E + \left.\frac{\partial\mathbf{D}}{\partial\nu}\right|_{n+\frac{1}{2}}\Delta\nu,$$

the notation $(\cdot)_{n+\frac{1}{2}}$ denotes quantities calculated so that their temperature dependence is accounted for, and $\boldsymbol{\varepsilon}_p$ is the plastic strain.

8 Thermomechanical Numerical Implementation

Given the relative ubiquity of information related to calculation of the purely mechanical problem (4.1)-(4.7), no further mention will be made to its general solution. The evolution of the thermomechanical solution is performed via a staggered, operator-split algorithm, as described in Box 1 for a single time step.

```
Data: Configuration at time n, solution fields and history variables at time n, time
      step size Δt
Result: Configuration at time n+1, solution fields and history variables at time n+1
begin
    for i_mm := 1, n_mm do
        for i_thermal := 1, n_thermal do
            Update element quantities and boundary conditions, based on latest
            configuration x_{n+1} and temperatures T_{n+1};
            Calculate thermal residual;
            Calculate temperature increment ΔT;
            Update temperatures T_{n+1};
            Calculate thermal convergence data;
            if thermal converged then
                exit thermal solution loop;
            end if
        end for
        for i_mech := 1, n_mech do
            Update element quantities and boundary conditions, based on latest
            configuration x_{n+1} and temperatures T_{n+1};
            Calculate mechanical residual;
            Calculate displacement increment Δu;
            Update displacements u_{n+1} and configuration x_{n+1};
            Calculate mechanical convergence data;
            if mechanical converged then
                exit mechanical solution loop;
            end if
        end for

        Calculate multi-mechanics convergence data;
        if multi-mechanics converged then
            exit multi-mechanics solution loop;
        end if
    end for
    if not multi-mechanics converged then
        reduce time step, and start over
    end if
end
```

Box 1: Algorithm used to calculate thermomechanical solution over an interval $(t_n, t_{n+1}]$

9 Thermomechanical Material Parameters

The material considered in the examples in the next section is 316L stainless steel. The property definitions used are recorded here for completeness. For each property, a plot is presented, and the values specified for the runs in the following section are explicitly listed. The values were taken from two primary sources, "Peckner" [22] and "Panos@UCSD" [23]. The "Diablo" input data was generated via interpolation (where data already existed) and extrapolation (no source considered had data over $\approx 1300\,K$ for any property).

It is noted that, in the process of researching the mechanical properties, more extensive data regarding the thermal properties was found.[2] As such, the thermal properties were also updated, and they are displayed first.

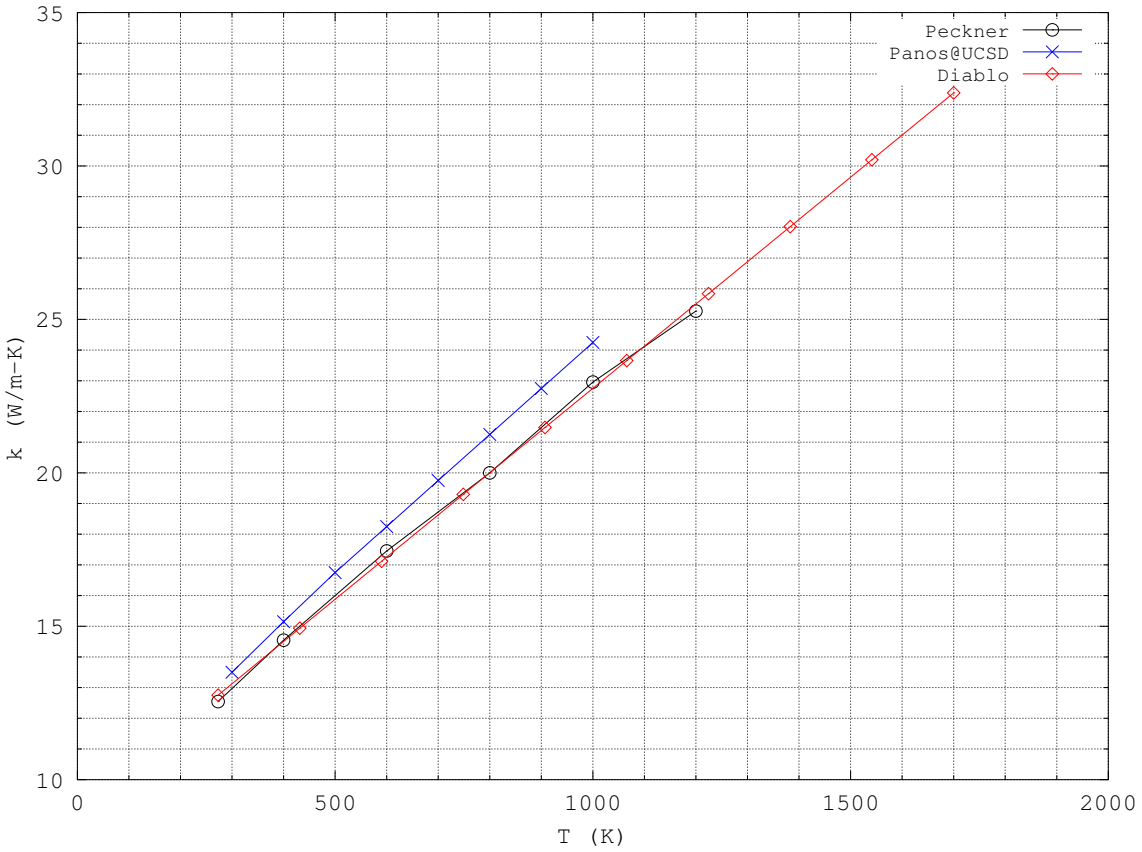

Figure 13: Thermal conductivity versus temperature

[2]Indeed, we envision further refinements of properties will occur as our research continues, but the values presented here are deemed sufficient to model the desired effects.

Table 3: Values of thermal conductivity versus temperature

Temperature $[K]$	Thermal conductivity $[W/m–K]$
273	12.76
432	14.94
590	17.18
749	19.30
907	21.48
1066	23.66
1224	25.84
1383	28.02
1541	30.20
1700	32.38

It is noted that the specific heat data contains two plots. The first contains the raw values, and this is the data that was used with the powder material and the Stefan-Neumann equation. The second shows the modified data, where points were added between $1650\,K$ and $1700\,K$ to account for the phase transition between solid and liquid phases, which was the data used for the consolidated material. The modification of the specific heat was described in [5] as "the latent heat is accounted for by increasing the heat capacity of the material in the phase change temperature range". The expression for the modified heat capacity is

$$c_{mod} = \frac{\left| \int_{T_s}^{T_l} c(T)\, dT + H \right|}{(T_l - T_s)},\ T_s < T < T_l,$$

where T_s, T_l are the solidus and liquidus temperatures, respectively. For the current case, the modified heat capacity is calculated as $6190\,J/kg–K$.

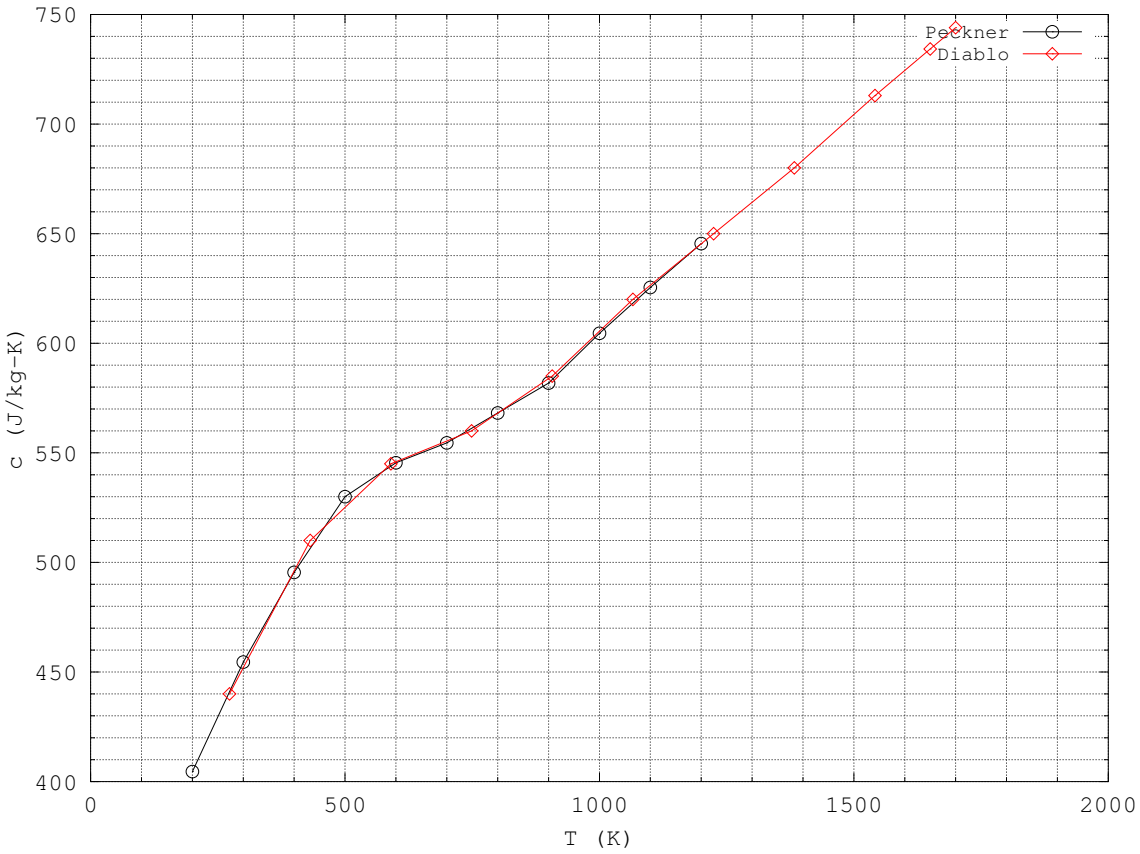

Figure 14: Specfic heat per unit mass (original data) versus temperature

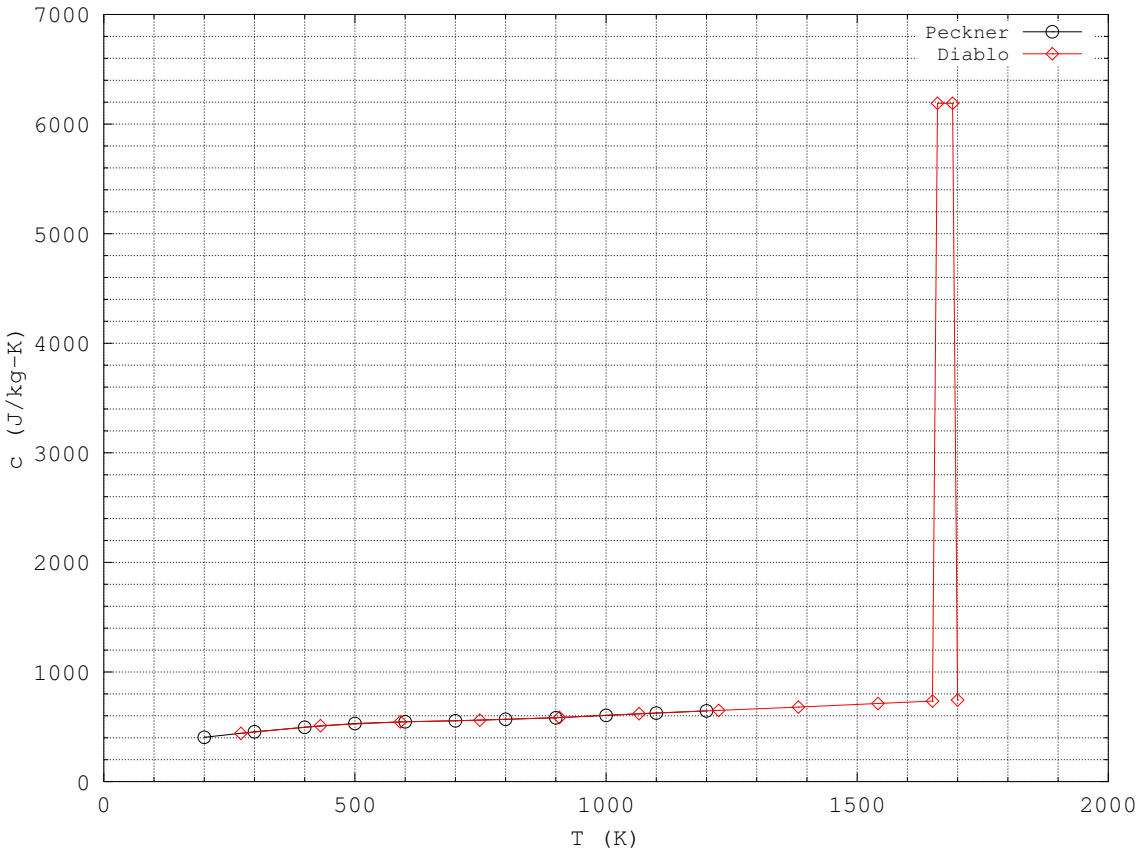

Figure 15: Specfic heat per unit mass (modified data) versus temperature

Table 4: Values of specific heat per unit mass versus temperature (* data is for the consolidated material only)

Temperature $[K]$	Specific heat per unit mass $[J/kg–K]$
273	440
432	510
590	545
749	560
907	585
1066	620
1224	650
1383	680
1541	713
1650	734
1660*	6190*
1690*	6190*
1700	744

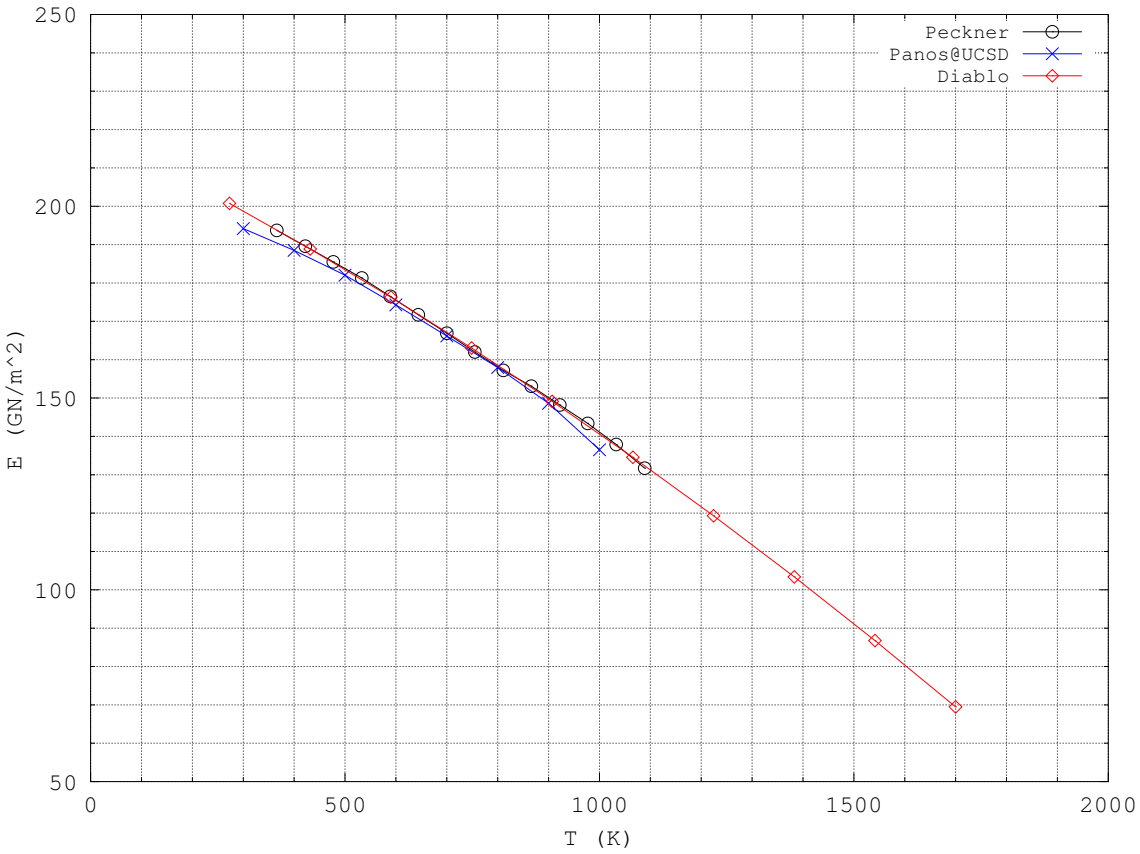

Figure 16: Young's modulus versus temperature

Table 5: Values of Young's modulus versus temperature

Temperature $[K]$	Young's modulus $[GPa]$
273	200.8
432	188.9
590	176.3
749	163.1
907	149.1
1066	134.6
1224	119.3
1383	103.4
1541	86.8
1700	69.5

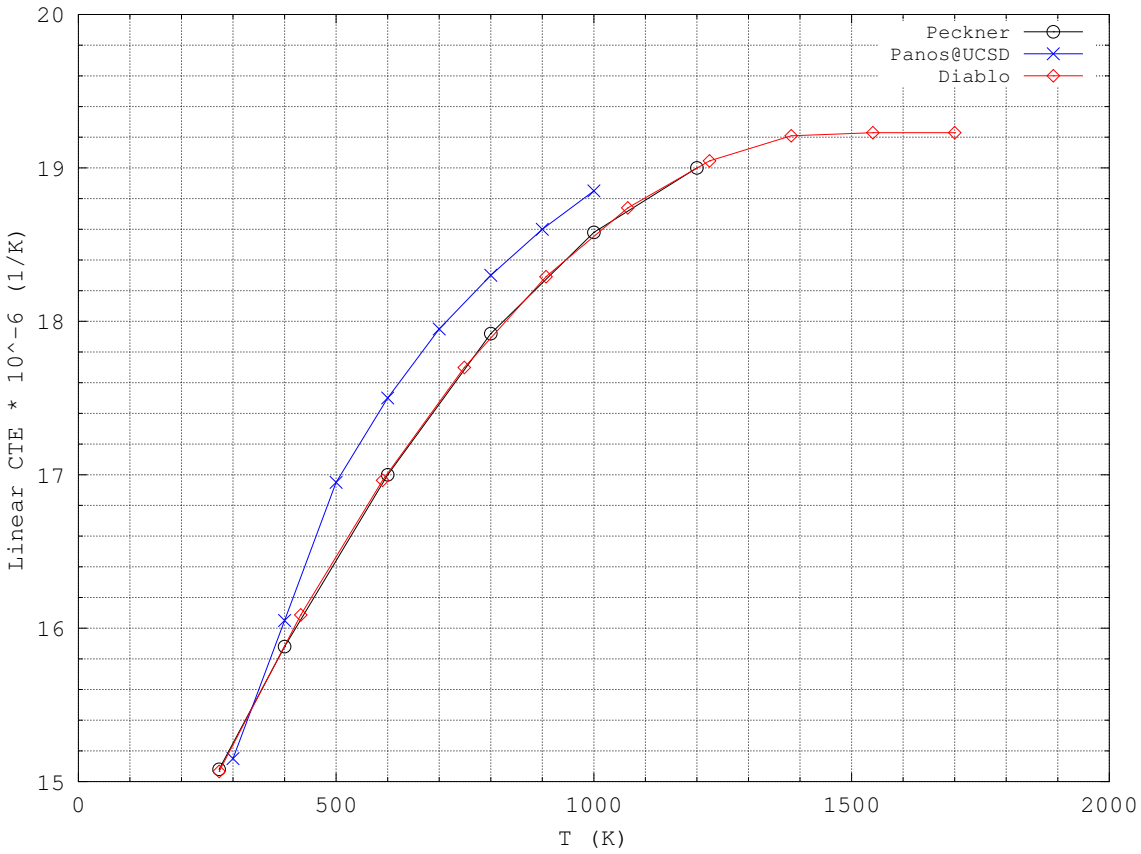

Figure 17: Linear coefficient of thermal expansion versus temperature

Table 6: Values of linear coefficient of thermal expansion versus temperature

Temperature $[K]$	Young's modulus $[10^{-6}/K]$
273	15.07
432	16.09
590	16.96
749	17.70
907	18.29
1066	18.74
1224	19.05
1383	19.21
1541	19.23
1700	19.23

The expression for the phase contraction coefficient for phase i can be expressed as

$$\beta_i = (\text{volume scale factor for phase } i)^{\frac{1}{3}} - 1.$$

Given volume scale factors of 1 and 0.6 for the powder and consolidated materials, respectively, the resulting phase contraction coefficients are $\beta_1 = 0$ and $\beta_2 = -0.15657$. Note that as utilized here, β_2 represents the contraction resulting from the total loss of porosity from the powder. Another physical mechanism is that of *solidification shrinkage*, a common concern for casting. Campbell [24] provides volume shrinkage data for common materials, listing pure iron as 3.16% and steels 3–4% depending on carbon content. By comparison, this effect in isolation would correspond to $\beta_2 \simeq -0.0118$. Given its comparitively small magnitude, for now we choose to consider this effect subsumed into the much larger value already indicated. At a later time, depending perhaps on results from powder scaling modeling, it may make sense to include this effect in the model.

The data regarding the yield stress and the tensile strength is presented in ratio form, where all values have been normalized by the yield stress/tensile strength (respectively) at room temperature.

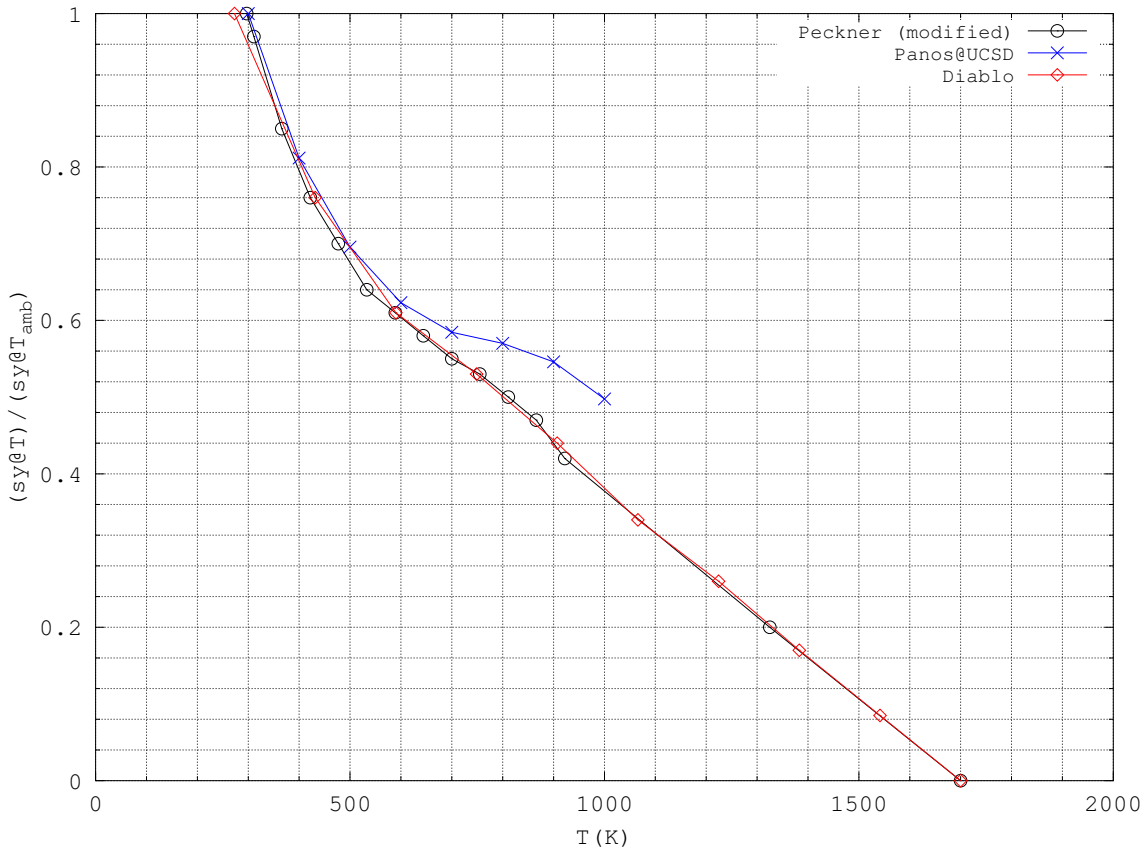

Figure 18: Yield stress ratio versus temperature

Table 7: Values of yield stress ratio versus temperature

Temperature $[K]$	Yield stress ratio
273	1.00
432	0.76
590	0.61
749	0.53
907	0.44
1066	0.34
1224	0.26
1383	0.17
1541	0.09
1700	0.00

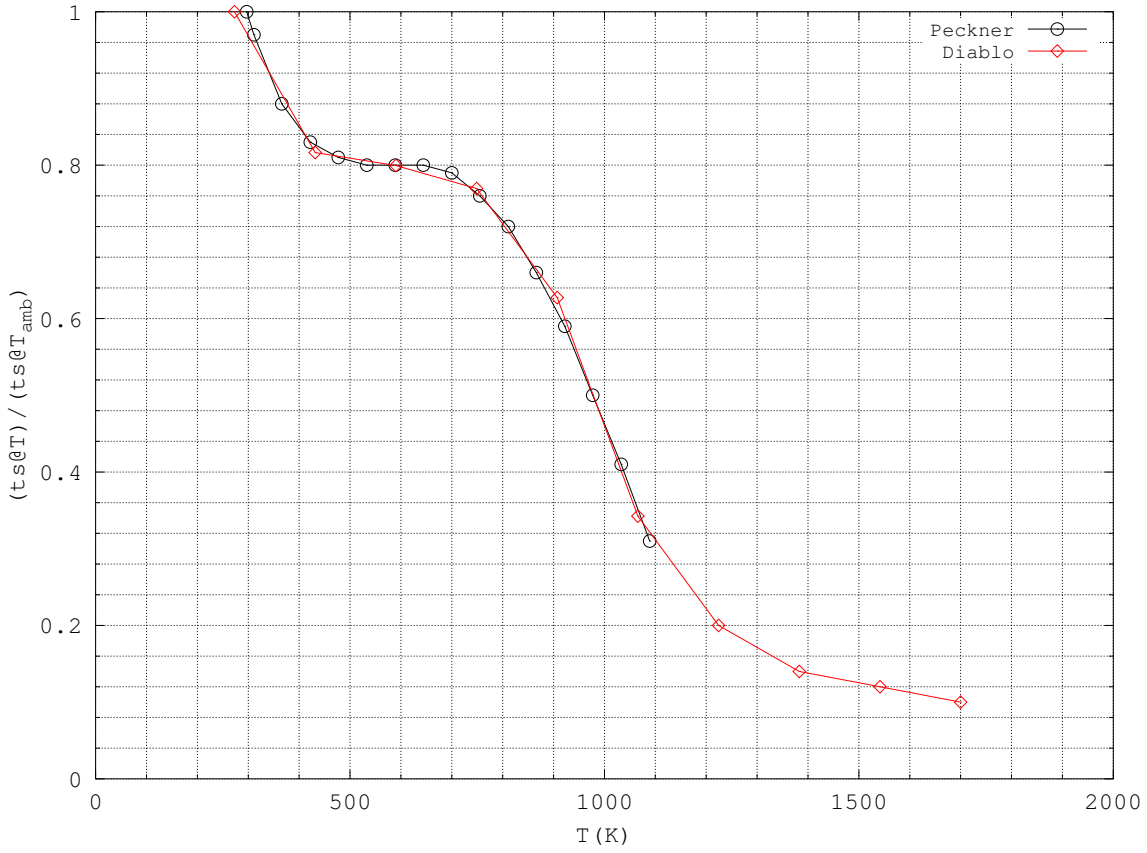

Figure 19: Tensile strength ratio versus temperature

It is noted that the tensile strength data is used solely for the computation of the plastic hardening modulus, and not to specify any kind of failure behavior.

Table 8: Values of tensile strength ratio versus temperature

Temperature $[K]$	Tensile strength ratio
273	1.00
432	0.82
590	0.80
749	0.77
907	0.63
1066	0.34
1224	0.20
1383	0.14
1541	0.12
1700	0.10

10 Thermomechanical Examples

The previously described algorithm for the coupled problem, and material properties, were used to compute the solution to several example problems intended to illustrate basic SLM behaviors at the continuum scale. The first problem consists of a baseplate with two layers being added. The results are presented in two cases. For both cases, the first layer fully phase changes, and the figure was generated just as the second layer was added. Both cases also have the same processing parameters, those being $Q_e = 33\,W$, $R = 0.060\,mm$, and $v = 180\,mm/s$. The first case illustrates the situation where no delay is specified between the two layers. In this case, the first layer is not completely consolidated, *i.e.*, although the phase transformation is complete, the volume change associated with the phase expansion coefficient has not completed. We attribute this to inertial effects and the result is clearly seen in the uneven thickness of the first powder layer (colored red in Figure 20).

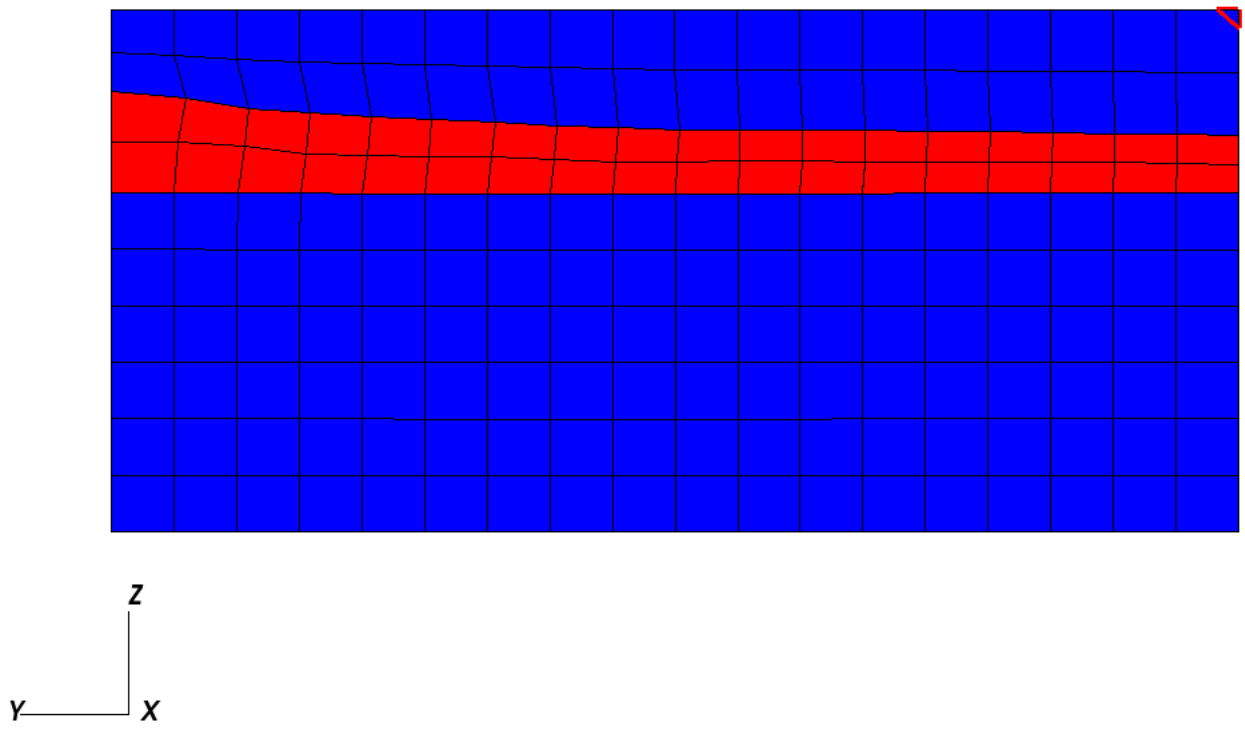

Figure 20: Two powder layers, with no time delay between

Alternately, for the case where a temporal delay was specified between the completion of the first layer and the activation of the second layer, the layer is fully consolidated, as illustrated in Figure 21. An immediate consequence of this is that the newly activated second layer has the desired uniform thickness.

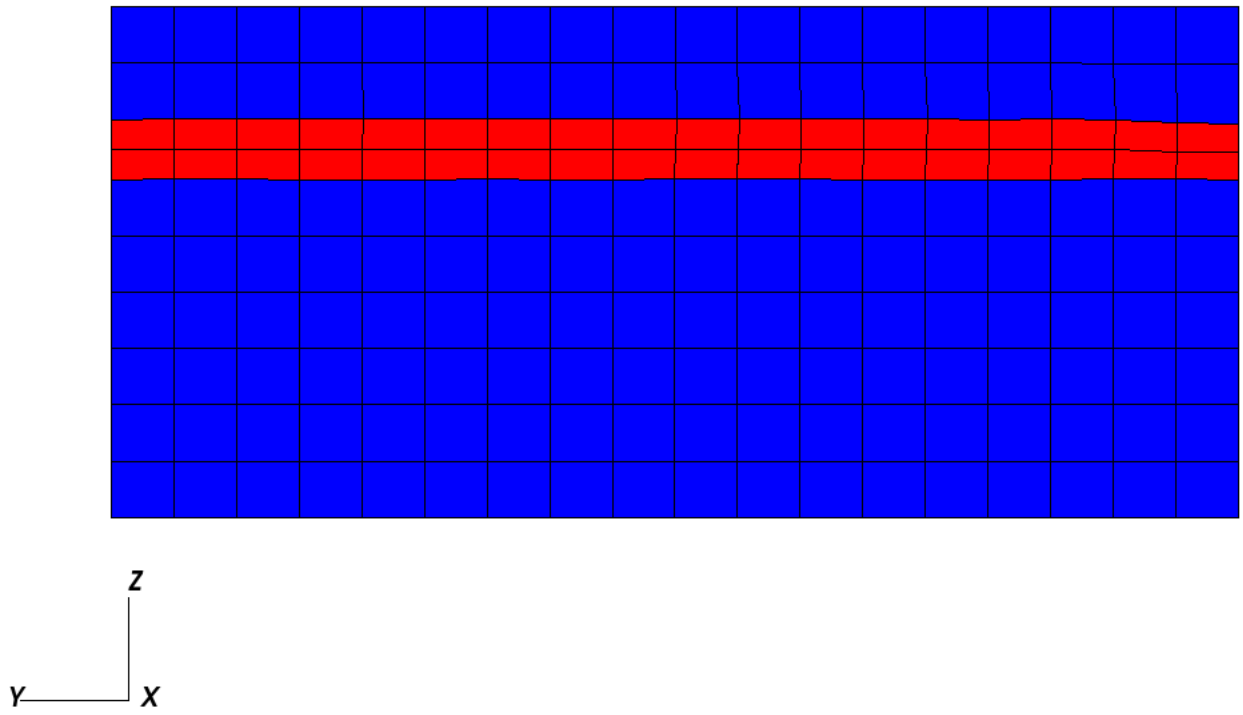

Figure 21: Two powder layers, with time delay between

The delay between the phase change and the volumetric consolidation can also be seen when looking at time-based data of the temperature and the displacement of a particular point, and an example of such data is shown in Figure 22. In the figure, the time lag bewteen the phase change (right after $0.02\,s$) and the completion of the volumetric consolidation (at, say, $0.09\,s$) is immediately apparent.

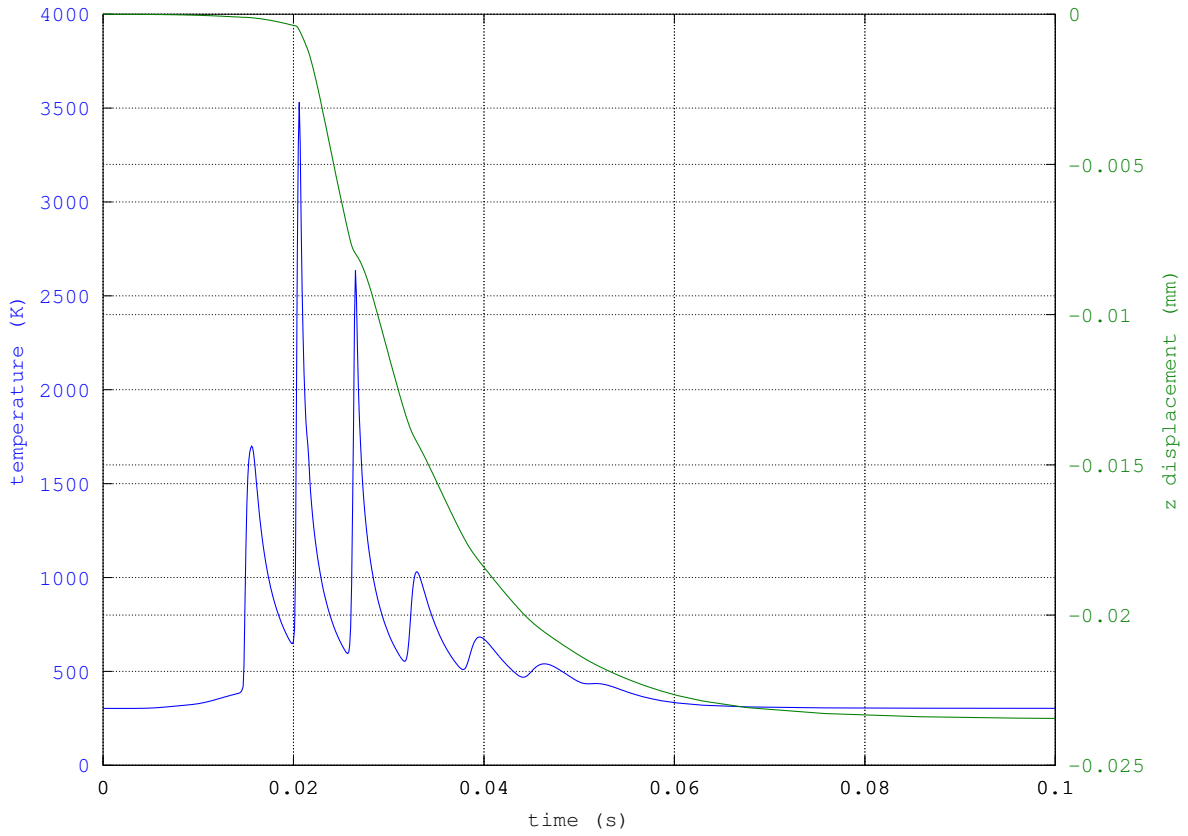

Figure 22: Time history of temperature and z displacement for a fixed node, illustrating the time scale of successive laser passes and eventual vertical consolidation

The second problem represents our initial attempt to calculate the solution over a somewhat larger domain, that being $1\,mm \times 1\,mm \times 1\,mm$. The external boundary conditions are $T = 303K$ at $z = 0$, and zero normal displacement on all faces, except $z = z_{max}$, which is specified as zero normal surface tractions. The initial conditions are uniform temperature $T = 303K$, and uniform displacement $\mathbf{u} = \mathbf{0}$ at the time of element activation. The heating path does not cover the entire $1\,mm \times 1\,mm$ cross-section in the $x - y$ plane; it only covers the area specified as $0.2 - 0.8\,mm \times 0 - 0.8\,mm$. That is, three sides of the heated area have an untransformed powder boundary of approximately $0.2\,mm$. As of the time of the writing of this report, the simulation had only completed 12 of the 20 powder layers. The following four figures provide a rough idea of the temporal progression of the problem. Readers with access to the LLNL internal network can view an animation of the cube example at

`https://acamm-dev.llnl.gov/newsletter/images/27October2013/phase_build.mpg`

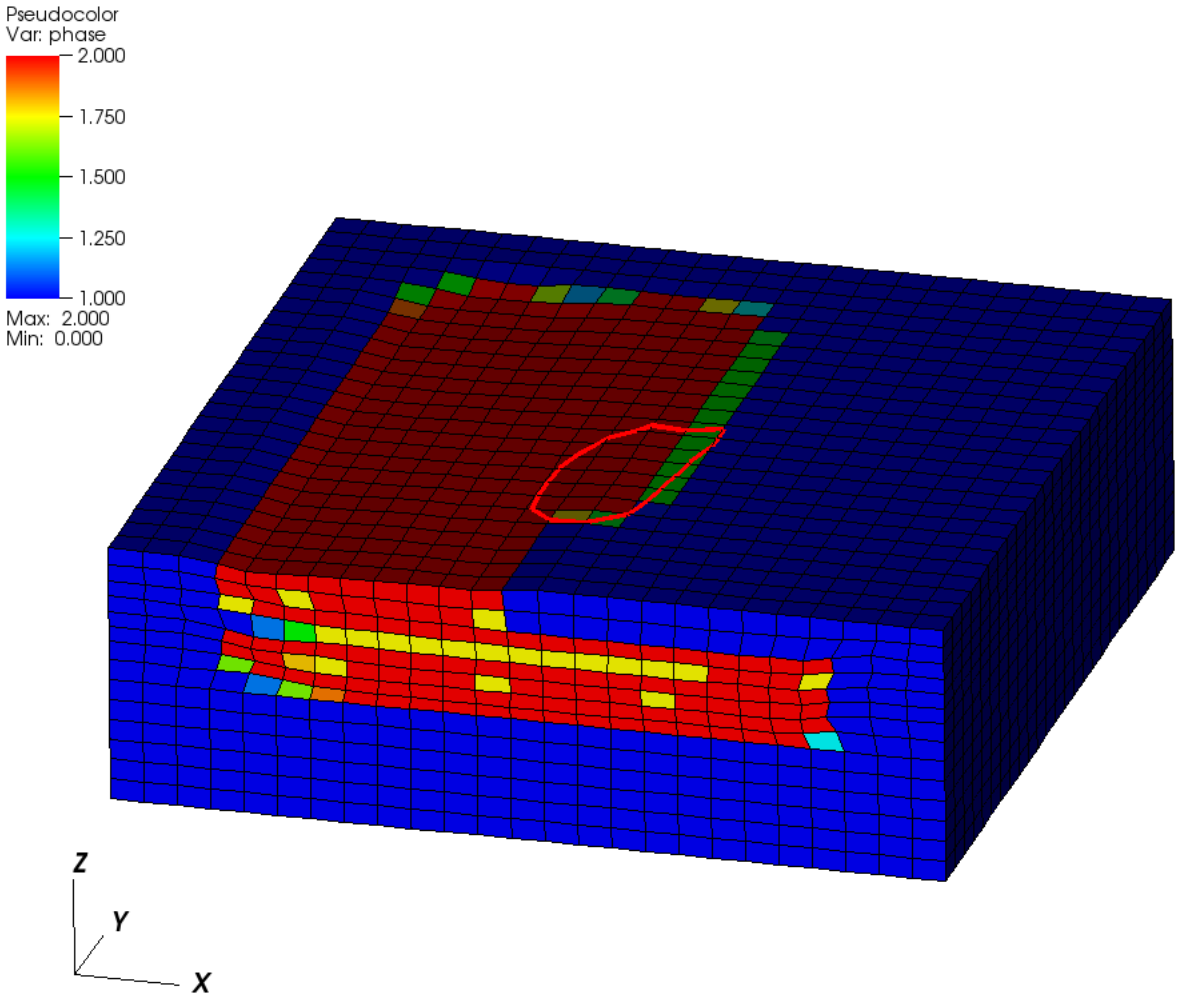

Figure 23: Cube example, layer 4, average phase $\bar{\phi}$ and contour of $T = 1700K$

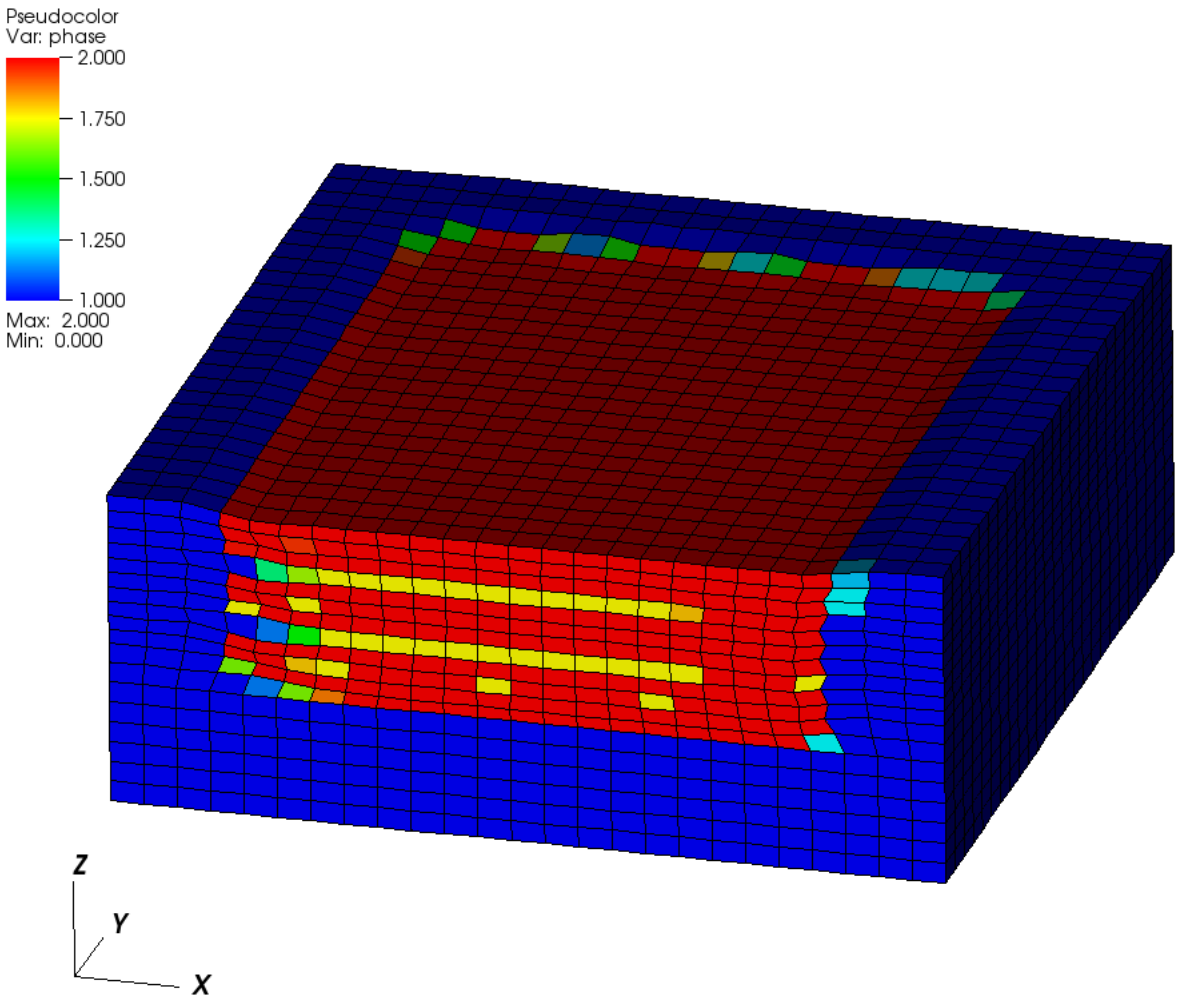

Figure 24: Cube example, between layers 6 and 7, average phase $\bar{\phi}$ and contour of $T = 1700K$

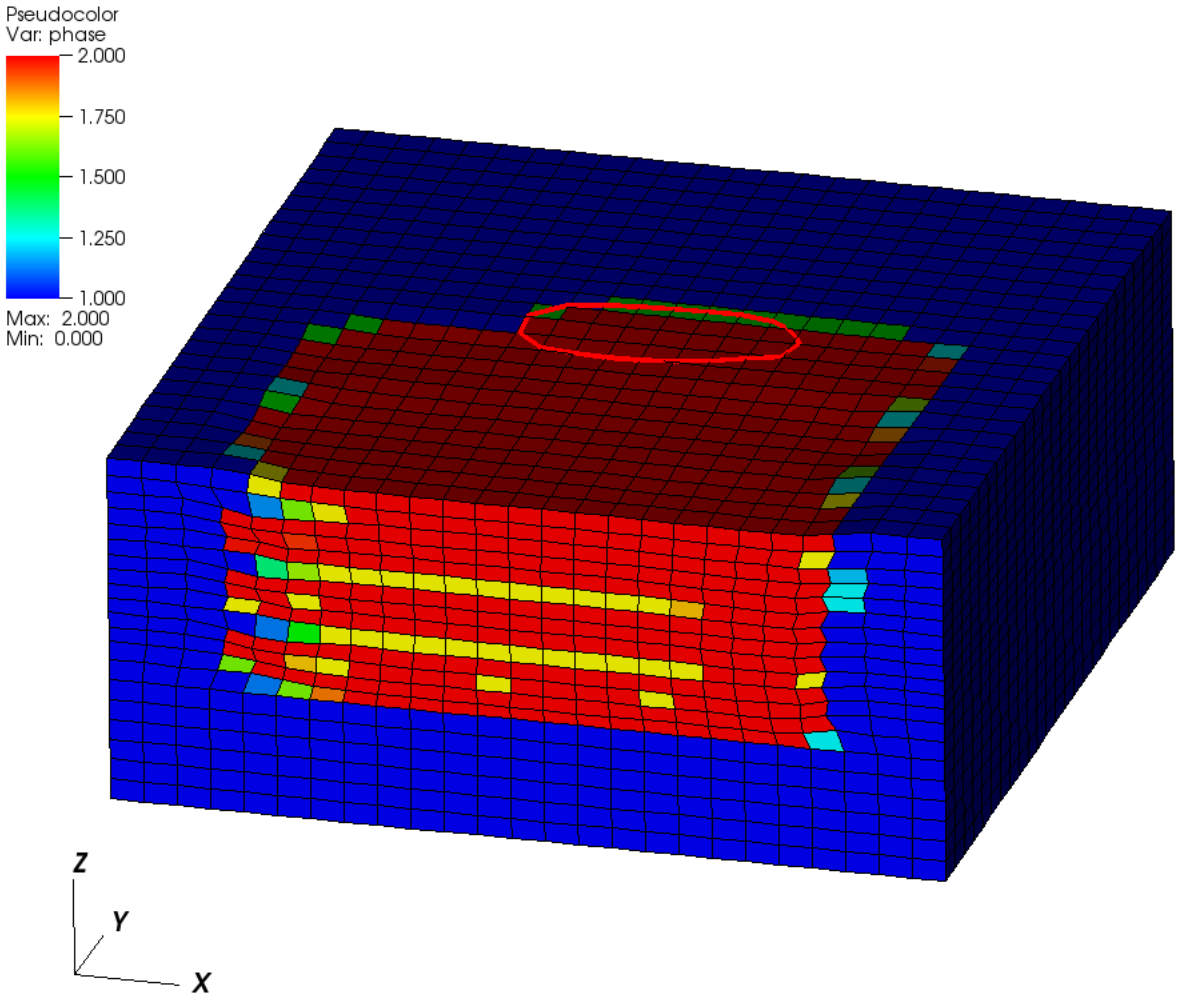

Figure 25: Cube example, layer 7, average phase $\bar{\phi}$ and contour of $T = 1700K$

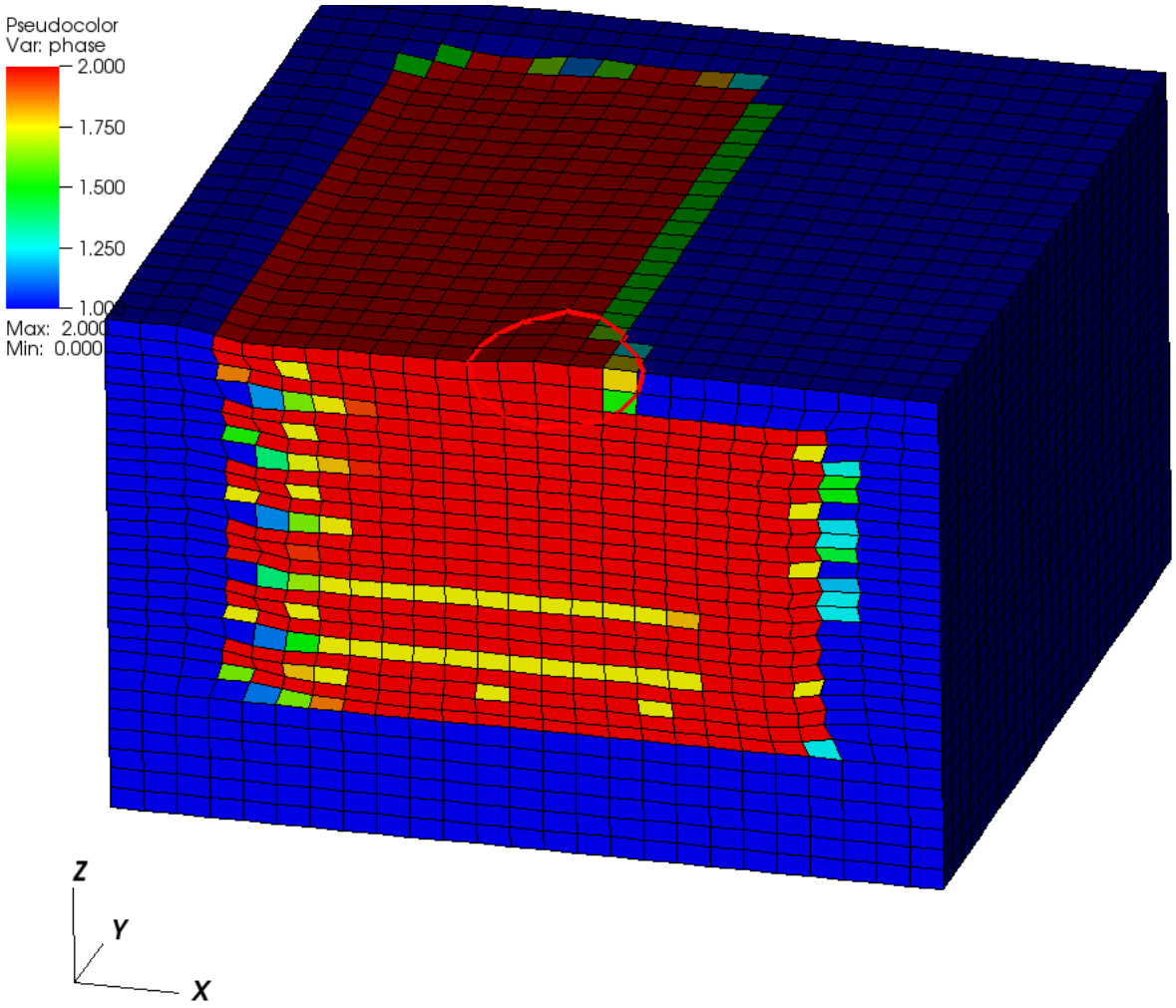

Figure 26: Cube example, layer 12, average phase $\bar{\phi}$ and contour of $T = 1700K$

While the domain is nowhere large enough to comment on part-scale response, several interesting observations can be made concerning the predicted stresses. Broadly speaking, stresses on the order of $\pm 100\, MPa$ are seen throughout the body, which is in rough agreement with LLNL's experimental experience to date [25]. We note that with this model we are seeing some "checkerboarding" in the element response which requires further investigation, so we will focus on trends rather than pointwise values. Figures 27-28 display the normal stresses in the X (left-right) and Y (into the figure) directions. The figures are plotted with identical contour ranges. Figure 28 displays more extreme stresses in the Y direction. This trend is consistent with there being less restraint applied in the X direction by virtue of both the shorter scan length and the existence of two powder boundaries. Figure 28 also shows a strong gradient in stress between compression in the base plate and tension in the upper layers of consolidated materials. Figure 29 illustrates the stresses in the Z (vertical build) direction. In particular, it shows large compression under the center of the build area that fall away in all lateral directions. This is another result that is consistent with empirical experience that build plates must resist warping forces from the SLM part. However, given that only a thin "veneer" of a real build plate is being modeled, and it is held with rigid

vertical diplacement boundary conditions at its bottom, we should not ascribe too much confidence in these specific numerical results.

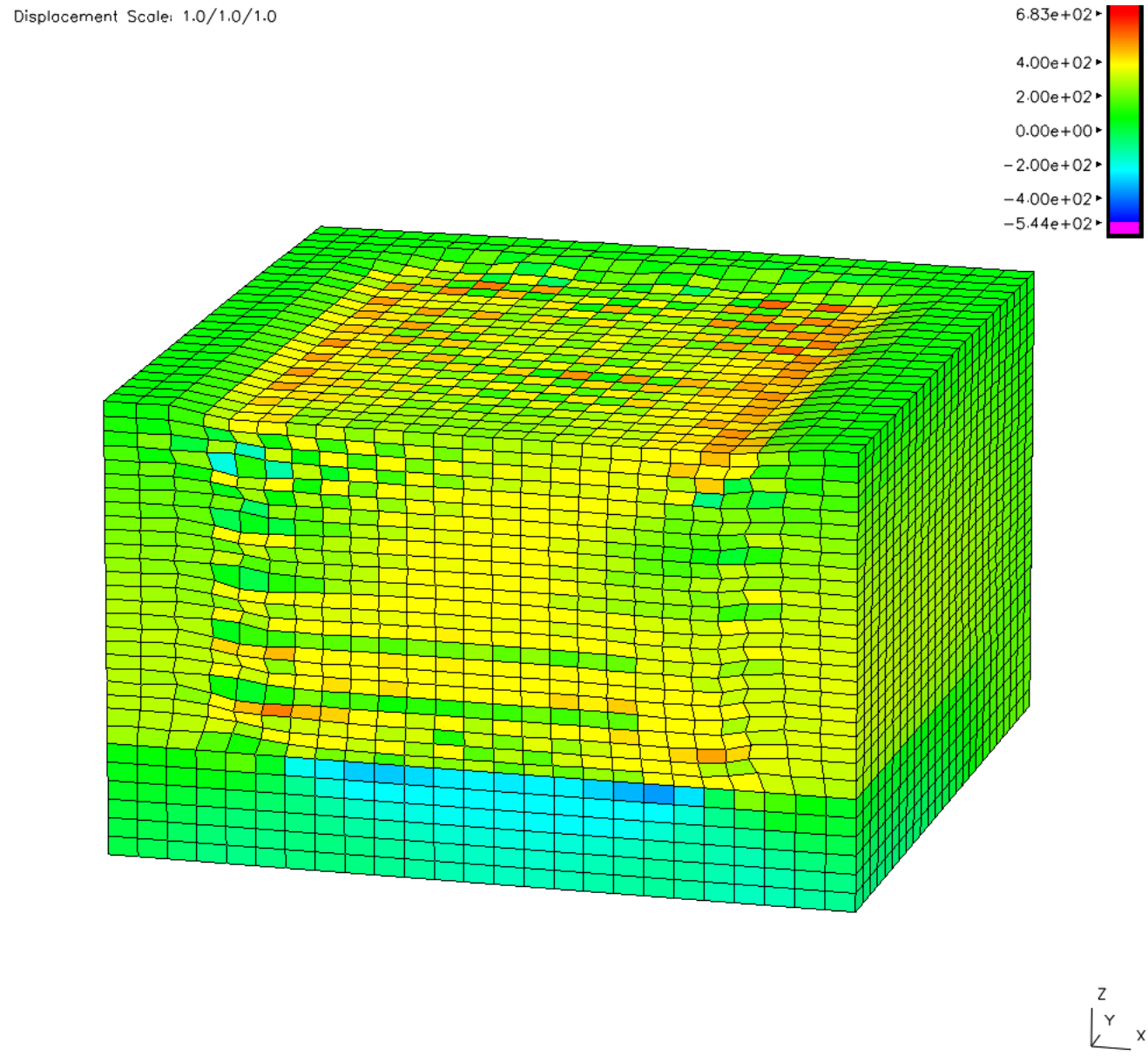

Figure 27: Cube example after 12 layers deposited, T_{xx} stress $[MPa]$. Contour range identical to that used in Figure 28.

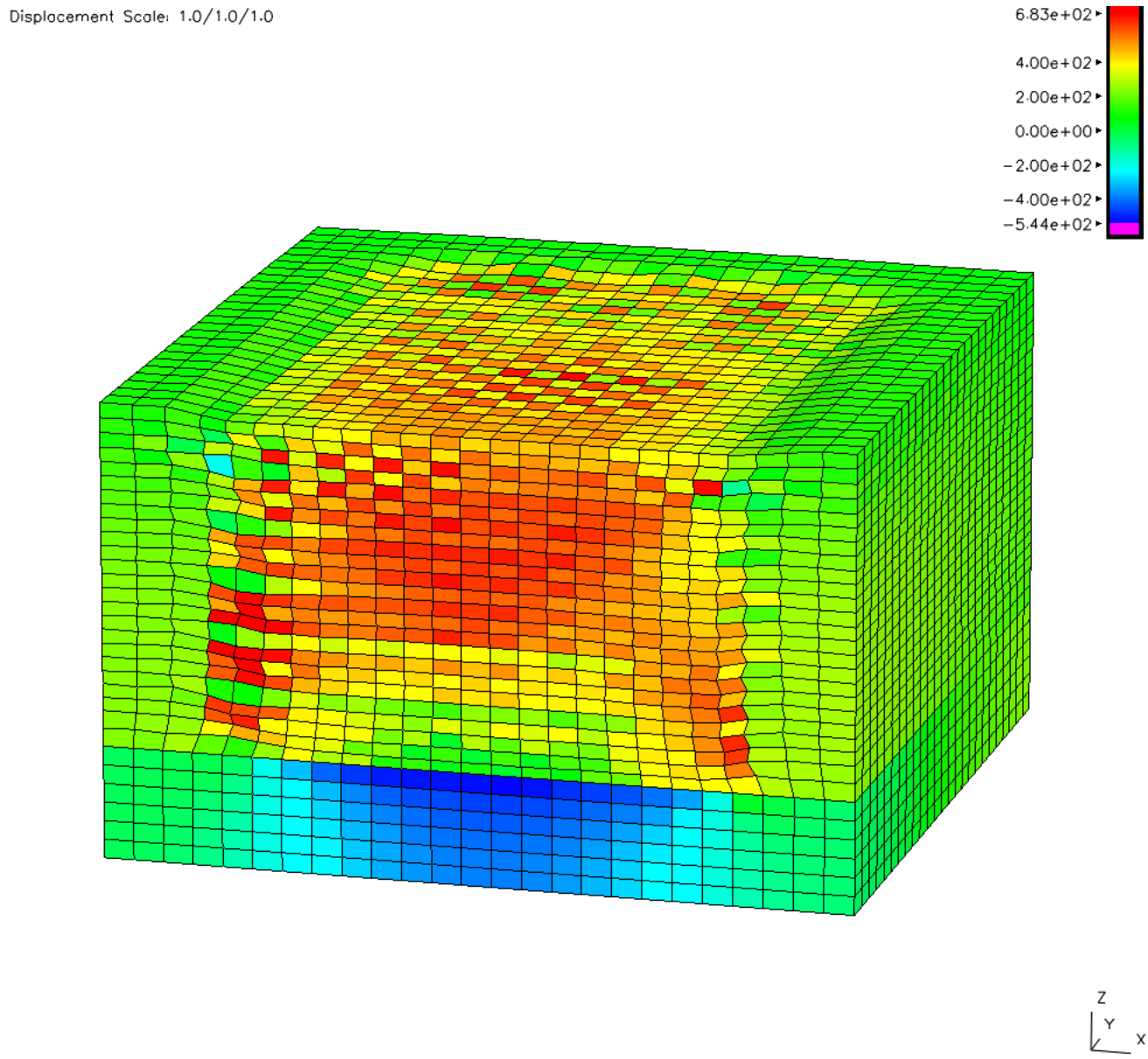

Figure 28: Cube example after 12 layers deposited, T_{yy} stress $[MPa]$.

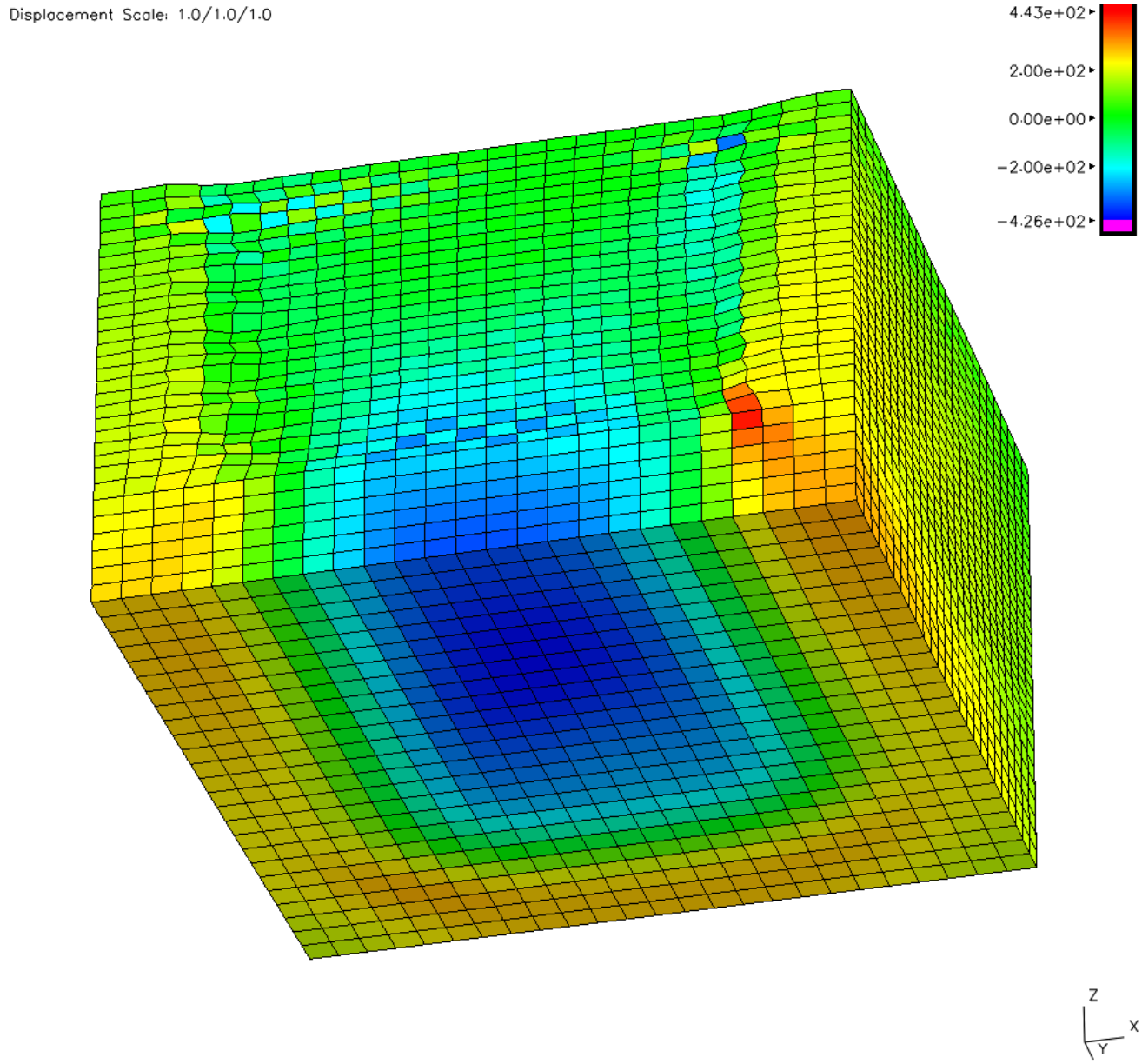

Figure 29: Cube example after 12 layers deposited, T_{zz} stress $[MPa]$.

The final comments regarding this larger domain example are with respect to the dynamics observed at representative locations. Figure 30 illustrates five points sharing a common in-plane location, but at different vertical positions corresponding to the build plate and the tops of layers 3, 6, 9 and 12. Figure 31 shows the history of temperatures at these points. The graph is truncated at 2000 K; this permits us to concentrate on the multi-layer dynamics rather than the peaks. The graph makes apparent when each layer is processed, but also reveals that each layer undergoes substantial thermal excursions during the processing of layers above it.

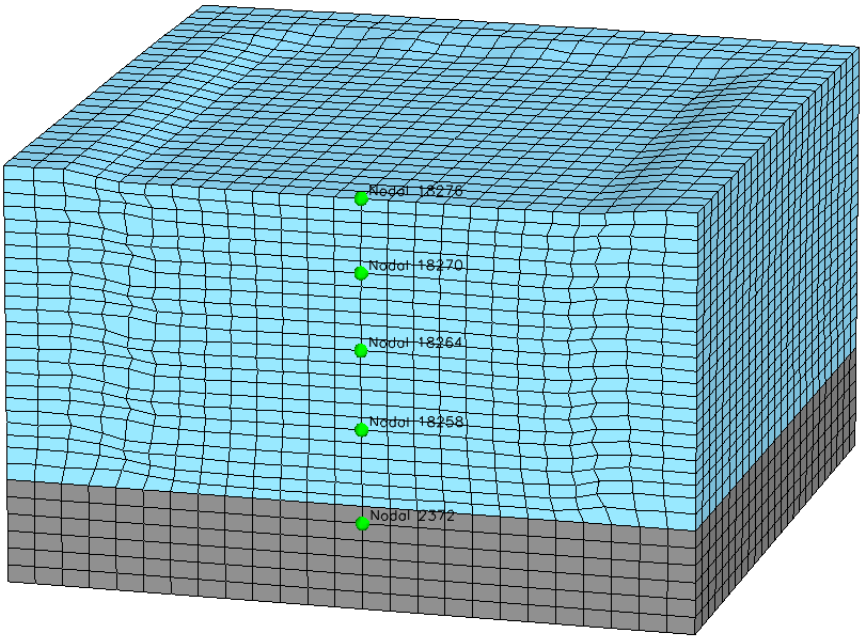

Figure 30: Temperature history sampling points subsequently labelled (bottom-to-top) as "base" and "layers" 3, 6, 9 and 12.

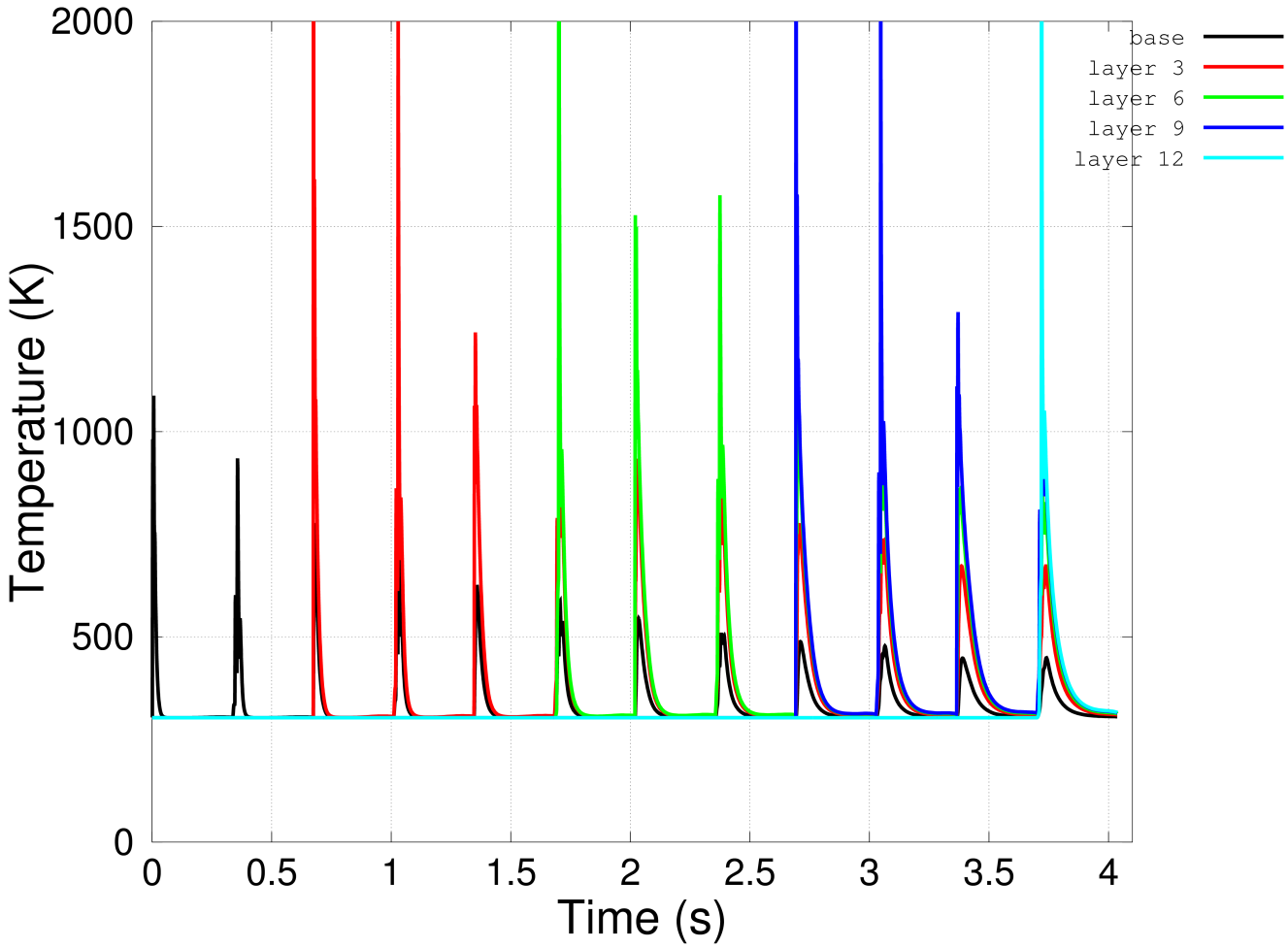

Figure 31: Temperature history for five sampling points designated in Figure 30.

The thermal interplay of layers is clearer if we zoom in on the time frame of processing a single layer. In Figure 32 we isolate on the processing of layer 12. The time at which the chosen position of layer 12 is being melted and consolidated is obvious enough. It is interesting to see that both layers 6 and 9 show effects from not just the laser track directly above the sampling point, but ajacent tracks as well. Referring back to Figure 28 for coordinate system orientation, layer 12 is processed using laser scans sweeping in the $\pm y$ -direction, with tracks "stacking up" in the $+x$ -direction. Hence, three laser tracks pass in the vicinity of the layer 12 sampling location. Indeed, the histories for layer 6 and 9 show three distinct peaks, with the strongest effect, not surprisingly, from the scan that passes nearest directly overhead.

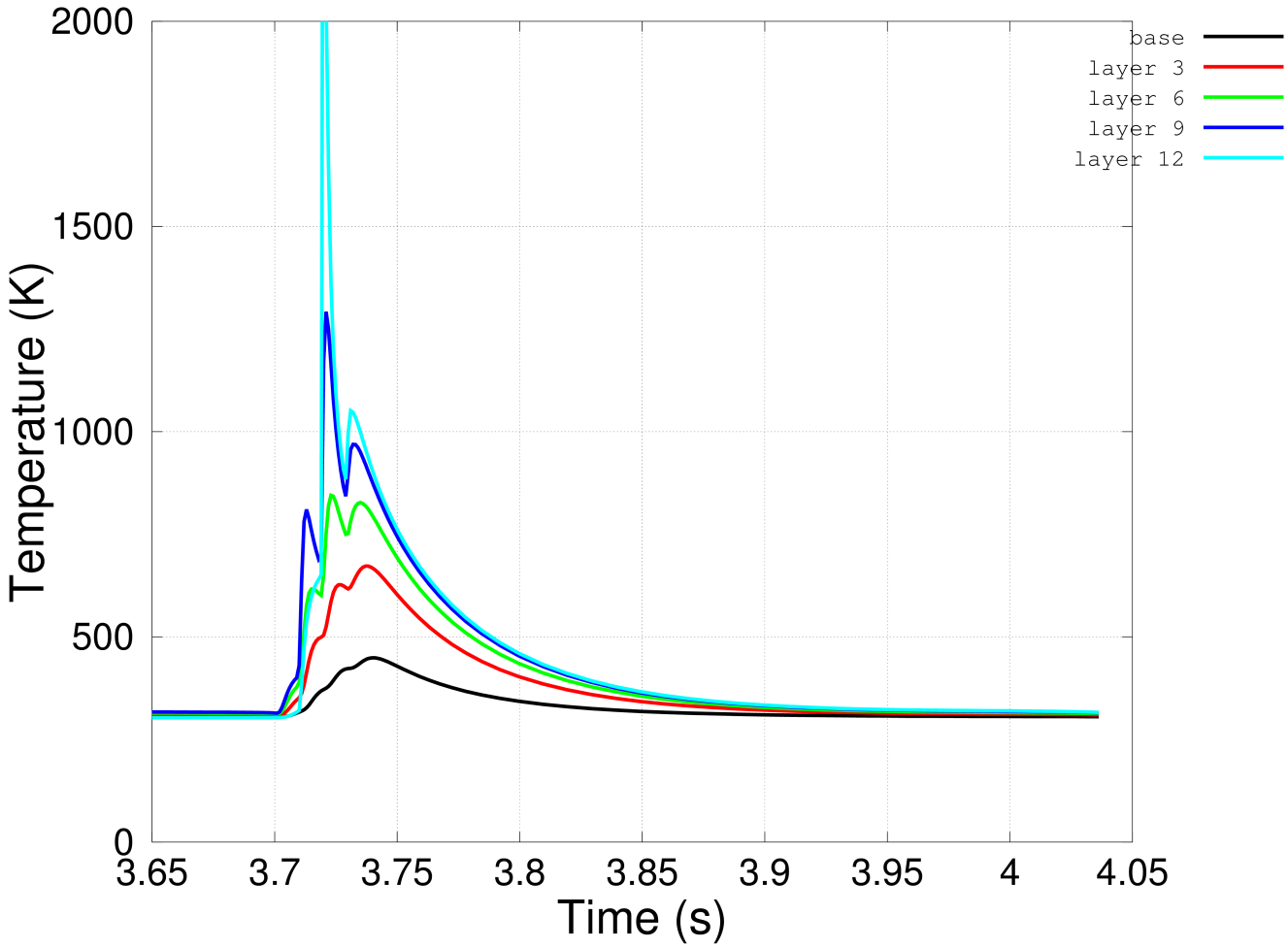

Figure 32: Temperature history restricted to time of layer 12 consolidation.

The overarching message from Figure 32 is that while the strongest thermal transformation of the material takes place during its layer scan, there is follow-on history that can be relevant. The figure shows that while processing layer 12, layer 9 is being driven to temperatures in the range of $0.75\,T_{\text{liquidus}}$. Obviously then the effects in the intervening material (layers 10 and 11) must be even stronger. We computed the (central difference) time derivative of temperature for the layer 9 location and plotted it in Figure 33. This demonstrates that material several layers below the active work surface is undergoing heating and cooling rates of order $10^5 K/\text{sec}$. This would appear to indicate that material microstructure will evolve over a series of layer consolidations and is consistent with the observation of grain sizes that are larger than individual powder layers [26].

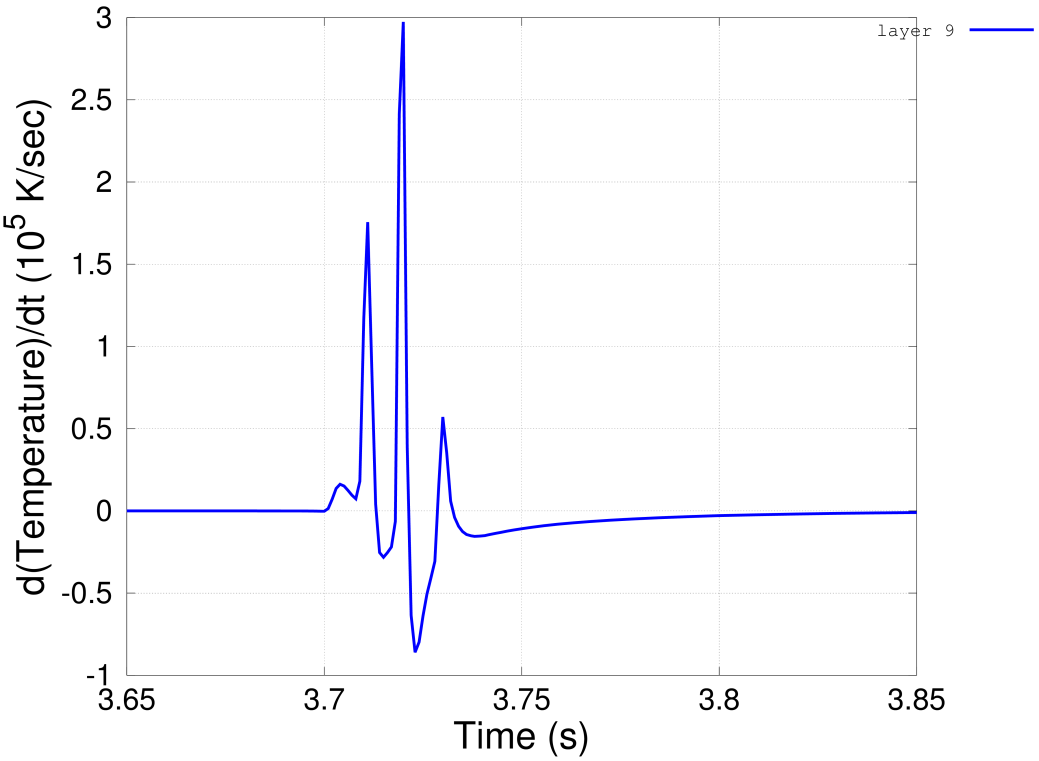

Figure 33: Temperature rate history for layer 9 sampling point restricted to time of layer 12 consolidation.

In closing we briefly consider mechanical history. We sampled elements adjacent to the in-plane location previously illustrated in Figure 30. Data for both elements in each layer were gathered and thus for clarity we plot the odd- and even-numbered layers in separate Figures 34-35. The histories all show a large effective plastic strain accumulated with the processing of their layer. This is consistent with the fact that the material is undergoing the large dilitational phase change (β_2) we use to model the consolidation of powder porosity during melt. However, under the interactions between an element and its neighbors, the

transformed elements are most free to deform uniaxially in the vertical (build) direction. Thus the bulk contraction, after overcoming the inertial lag noted earlier, is resolved to (primarily) uniaxial deformation via a large deviatoric response. With the current model this is thus realized as high plastic strains from flow associated with a very low yield stress and hardening modulus at near-melt temperatures.

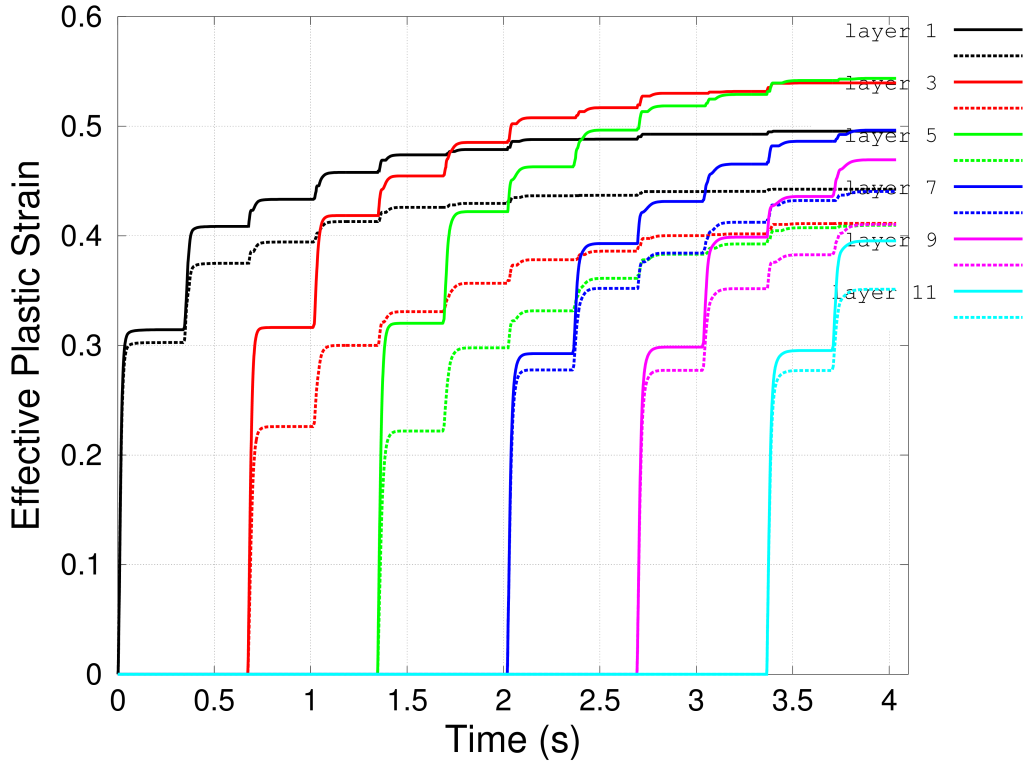

Figure 34: Measure of distortion for two elements sampled for each for odd-numbered layers. The lower element in each layer is plotted as a dotted line.

Figure 34 shows that most layers transform rather uniformly, whereas layers 3 and 5 show considerable thru-thickness variation. This is consistent with Figure 26, where yellow bands in the lower parts of layers 3 and 5 indicate the phase transformation was not driven to completion. Given that the laser scan was intended to be identical for all odd layers, this difference in behavior is not totally understood. First note that the elements sampled for the odd layers are processed by the very first laser scan for their layer. Thus if our process parameters are marginal for total melt, these would be among the most susceptible volumes of material. It can be argued that higher layers, being further from the thermal sink at the bottom of the build plate might benefit from longer dwell time at elevated temperature, leading to more homogeneous consolidation. Furthermore, elements in layers 3 and 5 having failed to fully transform, would have lower conductivity than the fully consolidated material and thus momentarily trap energy that would help layers 7, 9 and 11 fully transform. These effects begin to paint a self-consistent picture across the sampling points for odd layers,

with the exception of layer 1. Under the current interpretation it is not clear why there is through-thickness homogeneity there. The histories collectively show successive increments of deformation being accumulated during processing of layers above, with some hints of asymptotic values being approached.

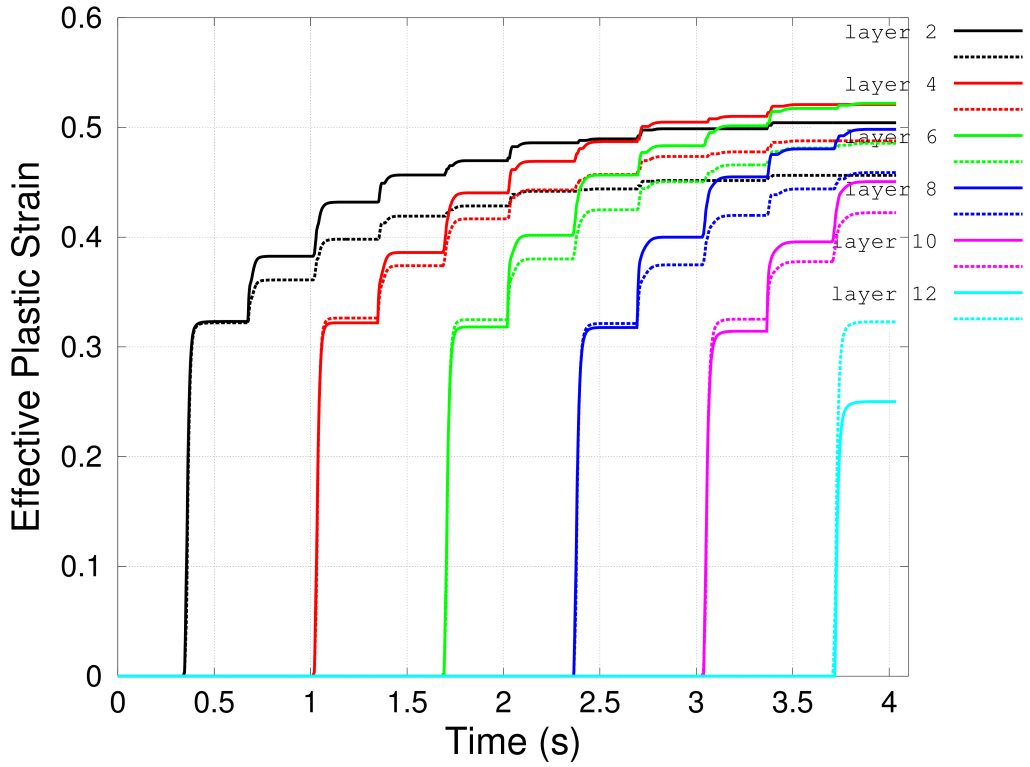

Figure 35: Measure of distortion for two elements sampled for each even-numbered layers. The lower element in each layer is plotted as a dotted line.

With Figure 35 we see considerable through-thickness homogeneity during the processing of layers 2, 4, 6, 8 and 10. This would be consistent with the thermal history discussion noting that for even-numbered layers, these sampling points correspond to locations benefiting from the proximity of three scans that are either ending or beginning in their vicinity. The response at layer 12 is not fully understood at this time. The trend has been confirmed by looking at results from multiple runs. It is perhaps a cautionary tale to avoid over-interpreting results from a single element, especially just in light of its thermal history. We have looked at nearby element pairs in layer 12 and most show through-thickness homegenity similar to the the other curves in Figure 35. The post-melt consolidation results in a 'wave' of deformation sweeping across the surface of a layer, and any one element's deformation will be influenced by multiple factors.

11 Conclusions

An initial continuum thermomechanical model has been developed for calculation of the result of a SLM process. The model includes a volumetric heat source designed to represent the radiation transport of laser energy into a powder, as well as phase change of the powder into a consolidated material that takes into account the latent heat of melting. Verification of the laser heating model and resulting thermal response against published literature is presented. Examples in both thermal only and thermomechanical cases have yielded promising results. The thermal examples illustrate extremely long ($> 1\,mm$) melt pools, as well as a spatial gap between the contour $T = 1700K$ and the phase change region; both phenomena are associated with high laser velocities ($> 1,000\,mm/s$). The thermomechanical results illustrate the overhang effect, as well as the effects of inertial lag in delaying volumetric consolidation of melted powder. Multi-layer simulations demonstrate that local thermal histories are impacted by the processing of layers immediately above and result in multiple intervals of rapid cooling. The results presented in this report serve as a solid foundation for further work related to complete part-level modeling.

Experience gained in the course of the implementation of the current models and methods described herein is essential in informing the path toward. In particular, it is noted that the Bathe algorithm [15] for phase change requires significant resources, i.e., adequate nonlinear convergence dictates the use of extremely small time steps. Indeed, the resource-intensive nature of the algorithm has also been noted by [5]. As such, one task for the next phase of the project will be to implement a different phase change algorithm, with the goal of improving the efficiency of the calculation. Futhermore, we must explore alternative spatial representations to proceed with the simulation of configurations beyond the small representative volumes shown to date. Approaches here could include

- a traditional mesh adaptation, *a la* AMR,
- synthesis of a homogenized model such that, say, $1\,mm$-cubes would be the building block for part-scale simulation,
- advanced techniques such as embedded mesh descriptions that could permit a moving island of refinement encompassing the vicinity of the melt pool.

The methodology research must be dual-tracked with validation exercises leveraging our current capabilities and available experimental evidence.

References

[1] I.D. Parsons, J.M. Solberg, R.M. Ferencz, M.A. Havstad, N.E. Hodge, and A.P. Wemhoff. Diablo User Manual. UCRL-SM-234927, Lawrence Livermore National Laboratory, September 2007.

[2] B. A. Finlayson and L. E. Scriven. The method of weighted residuals - a review. *Applied Mechanics Reviews*, 19:735–748, 1966.

[3] K. J. Bathe, E. Ramm, and E. L. Wilson. Finite element formulations for large deformation dynamic analysis. *International Journal for Numerical Methods in Engineering*, 9(2):353–386, 1975.

[4] J. Goldak, A. Chakravarti, and M. Bibby. A new finite element model for welding heat sources. *Metallurgical Transactions B*, 15(2):299–305, 1984.

[5] H. Hu and S. A. Argyropoulos. Mathematical modelling of solidification and melting: a review. *Modelling and Simulation in Materials Science and Engineering*, 4(4):371–396, 1996.

[6] A. Sharma, V. V. Tyagi, C. R. Chen, and D. Buddhi. Review on thermal energy storage with phase change materials and applications. *Renewable and Sustainable Energy Reviews*, 13(2):318–345, 2009.

[7] O. C Zienkiewicz, R. L Taylor, and J. Z Zhu. *The Finite Element Method: Its Basis and Fundamentals*. Elsevier Butterworth Heinemann, sixth edition, 2005.

[8] O. C. Zienkiewicz and R. L. Taylor. *The Finite Element Method: For Solid and Structural Mechanics*. Elsevier Butterworth Heinemann, sixth edition, 2005.

[9] G. A. Holzapfel. *Nonlinear Solid Mechanics: A Continuum Approach for Engineering*. Wiley, 2000.

[10] C.A. Felippa and K.C. Park. Staggered transient analysis procedures for coupled mechanical systems: Formulation. *Computer Methods in Applied Mechanics and Engineering*, 24(1):61–111, October 1980.

[11] C. Farhat and M. Lesoinne. Two efficient staggered algorithms for the serial and parallel solution of three-dimensional nonlinear transient aeroelastic problems. *Computer Methods in Applied Mechanics and Engineering*, 182(34):499–515, February 2000.

[12] A. V. Gusarov, I. Yadroitsev, Ph. Bertrand, and I. Smurov. Model of radiation and heat transfer in laser-powder interaction zone at selective laser melting. *Journal of Heat Transfer*, 131(7):072101, 2009.

[13] A. J. Dalhuijsen and A. Segal. Comparison of finite element techniques for solidification problems. *International Journal for Numerical Methods in Engineering*, 23(10):1807–1829, 1986.

[14] D. Poirier and M. Salcudean. On numerical methods used in mathematical modeling of phase change in liquid metals. *Journal of Heat Transfer*, 110(3):562, 1988.

[15] W. D. Rolph and K. J. Bathe. An efficient algorithm for analysis of nonlinear heat transfer with phase changes. *International Journal for Numerical Methods in Engineering*, 18(1):119–134, 1982.

[16] M. M. Vainberg. *Variational Methods for the Study of Nonlinear Operators*. Holden-Day, San Francisco, 1964.

[17] M. Z. Nashed. Some Remarks on Variations and Differentials. *American Mathematical Monthly*, 73(no. 4, part 2):63–76, 1966.

[18] J. L. Nowinski. Note on the applications of the Frechet derivative. *International Journal of Non-Linear Mechanics*, 18(4):297–306, 1983.

[19] T. J. R. Hughes and K. S. Pister. Consistent linearization in mechanics of solids and structures. *Computers & Structures*, 8(3-4):391–397, 1978.

[20] C. Kamath. Private communication, 2013.

[21] S. Khairallah and A. Anderson. Private communication, 2013.

[22] D. Peckner. *Handbook of Stainless Steels*. McGraw-Hill, San Francisco, CA, 1977.

[23] P.J. Karditsas and M.-J. Baptiste. Thermal and structural properties of fusion related materials, September 2013.

[24] J. Campbell. *Complete Casting Handbook: Metal Casting Processes, Metallurgy, Techniques and Design*. Butterworth-Heinemann, 2011.

[25] A. Wu. Private communication, 2013.

[26] B. El-dasher. Private communication, 2013.